PCYT2-regulated lipid biosynthesis is critical to muscle health and ageing

DOI:
10.1038/s42255-023-00766-2

Document Version
Accepted author manuscript

Published in:
Nature Metabolism

PCYT2-regulated lipid biosynthesis is critical to muscle health and ageing

Domagoj Cikes[1]*, Kareem Elsayad[2], Erdinc Sezgin[3,4], Erika Koitai[5], Torma Ferenc[5], Michael Orthofer[1], Rebecca Yarwood[6], Leonhard X. Heinz[7], Vitaly Sedlyarov[7], Nasser Darwish Miranda[8,] Adrian Taylor[9], Sophie Grapentine[9], Fathiya al-Murshedi[10], Anne Abot[11], Adelheid Weidinger[11], Candice Kutchukian[13], Colline Sanchez[13], Shane J.F. Cronin[1], Maria Novatchkova[1], Anoop Kavirayani[2], Thomas Schuetz[1], Bernhard Haubner[1], Lisa Haas[14], Astrid Hagelkruys[1], Suzanne Jackowski[15], Andrey Kozlov[11,12], Vincent Jacquemond[13,16], Claude Knauf[16], Giulio Superti-Furga[7,17], Eric Rullman[18,19], Thomas Gustafsson[18], John McDermot[20], Martin Lowe[6], Zsolt Radak[5], Jeffrey S. Chamberlain [21,22], Marica Bakovic[8], Siddharth Banka[20,23], Josef M. Penninger[1,24]*

[1] IMBA, Institute of Molecular Biotechnology of the Austrian Academy of Sciences, Vienna, 1030; Austria

[2] VBCF, Vienna Biocenter Core Facilities, Vienna Biocenter, Vienna 1030; Austria

[3] MRC Weatherall Institute of Molecular Medicine, MRC Human Immunology Unit, University of Oxford, OX39DS, Oxford; UK
[4] Science for Life Laboratory, Department of Women's and Children's Health, Karolinska Institutet, 17165, Solna, Sweden
[5] University of Physical Education, Budapest; Hungary
[6] School of Biological Sciences, Faculty of Biology, Medicine and Health, University of Manchester, Manchester M13 9PT; UK
[7] CeMM Research Center for Molecular Medicine of the Austrian Academy of Sciences, Vienna; Austria
[8] Institute of Science and Technology Austria (IST Austria), 3400, Klosterneuburg; Austria
[9] University of Guelph, Guelph; Canada
[10] Department of Genetics, College of Medicine, Sultan Qaboos University, Muscat; Sultanate of Oman
[11] Enterosys SAS, Prologue Biotech, Labège; France
[12] Ludwig Boltzmann Institute for Experimental and Clinical Traumatology, AUVA Research Center, Donaueschingenstraße 13, 1200 Vienna; Austria
[13] Institut NeuroMyoGène, Université Claude Bernard Lyon 1, F69622 Villeurbanne; France
[14] IMP Research Institute of Molecular Pathology, Vienna, Austria
[15] St. Jude Children's Research Hospital, Memphis, TN 38105-3678; USA
[16] INSERM U1220 Institut de Recherche en Santé Digestive, CHU Purpan, Université Toulouse III Paul Sabatier Toulouse; France
[17] Center for Physiology and Pharmacology, Medical University of Vienna, Vienna, Austria
[18] Division of Clinical Physiology, Department of Laboratory Medicine, Karolinska Institutet, and Unit of Clinical Physiology, Karolinska University Hospital, Stockholm; Sweden
[19] Cardiovascular Theme, Karolinska Institutet, Karolinska University Hospital Huddinge, Stockholm; Sweden
[20] Manchester Centre for Genomics Medicine, St Mary's Hospital, Manchester University Hospital Foundation Trust, Oxford Road, Manchester, M13 9WL; UK
[21] Department of Neurology, University of Washington, Seattle, WA; USA
[22] Senator Paul D. Wellstone Muscular Dystrophy Specialized Research Center, University of Washington, Seattle, WA; USA

[23] Division of Evolution and Genomic Sciences, School of Biological Sciences, Faculty of Biology, Medicine and Health, University of Manchester, Manchester M13 9WL; UK

[24] Department of Medical Genetics, Life Science Institute, University of British Columbia, Vancouver; Canada

Keywords: *Lipids; Genetic Disease; Ageing; Progressive Muscle Weakness; Phosphatidylethanolamine; Membrane Physicochemical Properties; Mitochondria; Gene Therapy; Muscle rejuvenation*

***Correspondence**

domagoj.cikes@imba.oeaw.ac.at (D.C.),

josef.penninger@ubc.ca (J.M.P)

Abstract

Muscle degeneration is the most prevalent cause for frailty and dependency in inherited diseases and ageing. Elucidation of pathophysiological mechanisms, as well as effective treatments for muscle diseases, represents an important goal in improving human health. Here, we show that the lipid synthesis enzyme phosphatidylethanolamine cytidyltransferase (PCYT2/ECT) is critical to muscle health. Human deficiency in PCYT2 causes a severe disease with failure to thrive and progressive weakness. Pcyt2 mutant zebrafish and muscle-specific Pcyt2 knockout mice recapitulate the patient phenotypes, with failure to thrive, progressive muscle weakness and accelerated ageing. Mechanistically, muscle Pcyt2 deficiency affects cellular bioenergetics and membrane lipid bilayer structure and stability. PCYT2 activity declines in ageing muscles of mice and humans, and AAV-based delivery of PCYT2 ameliorates muscle weakness in Pcyt2 knockout and old mice, offering a therapy for rare disease patients and muscle ageing. Thus, PCYT2 plays a fundamental and conserved role in vertebrate muscle health, linking PCYT2 and PCYT2 synthesized lipids to severe muscle dystrophy and ageing.

Main

Skeletal muscle is the biggest organ in the human body, with essential roles in support, mobility and metabolism. Muscle degeneration, either as a result of inherited diseases[1], chronic diseases, or ageing[2] severely impairs the life quality, and health of millions of people. Complete understanding of pathophysiological mechanisms driving this pathology represents an important objective in medicine.

Eukaryotic lipidome is complex with a potential of generating up to 100 000 different lipids[3]. Differences among specific lipids occur at subcellular compartments, cell and tissue types[4]. Tissue-specific differences suggest that certain organs use specific lipid pathways for organ health and longevity.

In humans, genetic deficiency in phosphatidylethanolamine cytidyltransferase (PCYT2/ECT), the bottle neck enzyme in PE synthesis through the Kennedy pathway[5], leads to complex and severe hereditary spastic paraplegia (HSP)[6,7]. Here, we discover a conserved, essential and specific role for PCYT2 synthesized phosphatidylethanolamine (PE) in muscle health. *Pcyt2* mutant zebrafish and muscle specific *Pcyt2* knockout mice recapitulate several patient phenotypes, particularly failure to thrive, short stature, impaired muscle development, and progressive weakness, with accelerated ageing and shortened life span. In contrast, mice lacking Pcyt2 in other tissues appeared unaffected. Loss of PCYT2 in muscle results in alterations in the mitochondrial and cellular lipidome, affecting mitochondrial function and physicochemical properties of the lipid bilayer, compromising sarcolemmal stability and exercise tolerance. We further show that PCYT2 activity declines in aging muscles of humans and mice and that *Pcyt2* gene-therapy in *Pcyt2* knock-out and aged mice improved muscle strength. Thus, PCYT2 and PE synthesized via PCYT2, are essential to muscle health, linking mitochondrial and sarcolemmal lipid bilayer perturbations to muscle degeneration, exercise tolerance and aging.

Results

Patients with disease-causing *PCYT2* variants fail to thrive

PCYT2 mutations were recently discovered in patients who manifest a complex disorder that involves developmental gross motor delay and progressive overall muscle weakness[6]**.** Observing these patients, we found that those with a homozygous nonsense variant NM_001184917.2:c.1129C>T (p.Arg377Ter) in *PCYT2* exhibited an apparently lower weight and shorter body length from birth, throughout childhood, and adulthood (Figure 1A,B). We also assessed patients with mutations in *EPT1*, which encodes the final enzyme in PE synthesis via the Kennedy pathway (Extended Figure 1A,B). These patients manifest similar clinical features as those with *PCYT2* mutations[7,8]. Indeed, patients with a homozygous variant NM_033505.4:c.335G>C (p.Arg112Pro) in EPT1 also exhibited growth defects, further confirming a role for the Kennedy pathway in postnatal growth (Extended Data Figure 1B). Thus, in addition to previously described symptoms, mutations in two critical enzymes that generate PE in the Kennedy pathway are associated with stunted growth.

Pcyt2 deficiency in zebrafish affects muscle and whole-body growth

Since Ept1 loss can be partially compensated by Cept1[9], we focused on the bottleneck enzyme PCYT2 (Extended Figure 1A). Given the ubiquitous tissue expression of PCYT2[10] (Supplementary Figure 3), its loss of function could potentially affect several organs, thus contributing to the complexity and severity of the disease. To gain insight into pathophysiological mechanisms, we first examined hypomorphic mutant *pcyt2* zebrafish[6]. Similar to the human rare disease patients, *pcyt2* mutant zebrafish were significantly smaller (Figure 1C).

Zebrafish and mouse models of hereditary spastic paraplegia rarely exhibit whole body growth phenotypes[11 12,13]. However, muscle development is essential for whole-body growth, and failure to thrive is a well-known feature of muscular dystrophies[14]. Therefore, we examined muscle morphology in *pcyt2* mutant zebrafish. We observed significantly smaller skeletal muscles, with smaller fibers without total number change in *pcyt2* mutant zebrafish (Figure 1D, Supplementary Figure 4A,B). These results suggest that impaired muscle

development could explain the stunted growth associated with *pcyt2* loss-of-function mutations in zebrafish and patients.

Pcyt2 muscle deficiency in mice impairs muscle and whole-body growth

In mice, global disruption of Pcyt2 results in embryonic lethality[15]. Therefore, to study the role of Pcyt2 in muscle health, we generated mice with muscle-specific *Pcyt2* deletion early during muscle development to recapitulate the human condition. We crossed *Pcyt2*$^{flox/flox}$ with *Myf5* promoter driven *Cre* mice to generate *Myf5Cre-Pcyt2* offspring, given that Myf5 is the first broadly expressed myogenic regulator in the developing myotome[16]. *Pcyt2* deletion was validated by RNA sequencing (Extended Data Figure 2A, *Myf5Cre-Pcyt2* mice were born at normal Mendelian ratios, but were significantly smaller at birth (postnatal day P1) and early postnatal days (P4), gained less weight, and grew less during the postnatal period compared to controls, as observed for both genders (Figure 1E,F; Extended Data Figure 3A-D). Neither *Myf5Cre* nor *Pcyt2*$^{flox/flox}$ littermate controls displayed a phenotype, therefore we used *Pcyt2*$^{flox/flox}$ littermates as controls for all subsequent experiments. We noticed that limb muscles were smaller in *Myf5Cre-Pcyt2* mice compared to controls already at P10 and at 2 months old (Figure 1G; Extended Data Figure 3E-H). Myofiber size was reduced in skeletal muscle (Figure 1G-I). Lipidomic analysis of quadriceps muscle isolated from 10-day old *Myf5Cre-Pcyt2* mice showed a marked reduction in the levels of PE, particularly of long-chain fatty acid PE species (Figure 1J, K). In addition, our data revealed an increase of PC lipids from the PC branch of the Kennedy pathway and upregulation of several enzymes from PE and PC branch of the Kennedy pathway (Figure 1J, Extended Data Figure 3I).

Muscle growth is mediated first by muscle satellite cell proliferation and an increase in myofibers until ~P7, and subsequently via myofiber hypertrophy[17]. The number of proliferating cells as well as the rate of myoblast proliferation was unaffected in the developing muscles and in myoblasts of *Myf5Cre-Pcyt2* mice (Extended Data Figure 4A, B). Although the number and distribution of Pax7^{+} muscle progenitor cells was similar in adult *Myf5Cre-Pcyt2* and control mice (Extended Data Figure 4C), *Myf5Cre-Pcyt2* mice showed a mild but significant reduction in myoblast fusion, with thinner myofibers (Figure 2A-C). Several pro-fusion and late differentiation markers were reduced in the myoblasts from *Myf5Cre-Pcyt2* mice (Figure 2D). There were no apparent changes in the levels of

transcriptional regulators of myofiber differentiation, such as MyoD and MyoG (Figure 2D). Membrane lipid composition is essential for myoblast fusion[18]. Given that PE lipids are abundant membrane lipids, we wanted to address if unavailable PE in the myoblast membrane would affect fusion into myofibers. We used the non-toxic, PE-specific SA-Ro binding probe[19] to mask the externally exposed membrane PE during myoblast fusion, mimicking PE deficiency. Indeed, myoblast fusion was severely affected (Figure 2E-G), showing that membrane PE is required for efficient myoblast fusion.

To directly examine hypertrophic growth independently of the myoblast fusion process, we performed synergic muscle ablation[20]. Muscle overloading resulted in a significant enlargement of the plantaris muscle on the un-operated limb in control mice but not in *Myf5Cre-Pcyt2* mice (Figure 2H). Phosphorylation of P-S6K1 and 4E-BP1, downstream markers and effectors of global protein synthesis and translation, appeared to be effective (Extended Data Figure 5A), indicating that impaired protein synthesis does not underlie the observed defect in hypertrophic growth of muscles from *Myf5Cre-Pcyt2* mice. The observed impaired myoblast fusion and hypertrophic muscle growth in *Myf5Cre-Pcyt2* mice did not affect the fiber type distribution nor fiber number in muscles from adult *Myf5Cre-Pcyt2* mice (Extended Data Figure 5B-D). Together these data show that loss of *Pcyt2* impairs long-chain fatty acid PE production and compromises both progenitor fusion and hypertrophic growth, leading to smaller myofibers and skeletal muscles.

Muscles lacking *Pcyt2* exhibit progressive wasting

We noticed that adult *Myf5Cre-Pcyt2* mice exhibited hindlimb clasping upon tail suspension (Figure 3A,B), indicative of muscle weakness. Indeed, muscle strength was reduced and progressively declined as *Myf5Cre-Pcyt2* mice aged (Figure 3C, Extended Data Figure 6A). At 8 months of age all *Myf5Cre-Pcyt2* mice developed kyphosis (Figure 3D), which was also seen in *PCYT2* disease patients (Figure 3E) and has been reported in mouse models of muscular dystrophy [21] . Atrophy of muscle tissue was evident in *Myf5Cre-Pcyt2* mice (Figure 3F) with a high incidence of central nuclei (Figure 3G). Furthermore, we observed tubular aggregates and inflammation in the muscles of 12-15 months old *Myf5Cre-Pcyt2* mice (Figure 3H, Extended Data Figure 6B-D). Consequent to the observed muscle weakness that was

apparent for both genders, *Myf5Cre-Pcyt2* mice developed secondary osteopenia contributing to overall frailty (Figure 3I) and reduced lifespan (Figure 3J).

As expected, progressive atrophy had a marked effect on whole-body metabolism. At 6 months of age, glucose clearance was increased with progressive decline in blood glucose levels and food consumption by 8 months of age (Extended Data Figure 6E-F, Supplementary Figure 5A,B) which could explain the increased mortality starting at this age. There were no apparent structural defects in respiratory muscles (Supplementary Figure 6). Although *Myf5Cre-Pcyt2* mice were less active (Extended Data Figure 6G), energy expenditure was significantly increased in both light and dark periods (Extended Data Figure 6H). Under thermoneutrality, during the light phase energy expenditure in *Myf5Cre-Pcyt2* mice was comparable to Control mice, while during the dark phase the higher energy expenditure was again evident (Extended Data Figure 6I). The lower activity and the muscle weakness of *Myf5Cre-Pcyt2* mice were also evident under thermoneutrality (Extended Data Figure 6J,K).

Pcyt2 is specifically required in muscle

Myf5Cre is active in precursors of both skeletal muscle and brown adipose tissue (BAT)[22]. PE species were reduced in the BAT of *Myf5Cre-Pcyt2* mice, but to a markedly lower extent than in the skeletal muscle, with an increase of PC lipids (Extended Data Figure 7A,B). Importantly, loss of *Pcyt2* and the observed lipid remodeling did not affect *in vitro* differentiation of adipocyte progenitors into brown fat, thermoregulation through BAT actvity, nor levels of Ucp1 in BAT (Extended Data Figure 7C-F). In addition, mitochondrial ultra-structures, content and respiration appeared normal in BAT of *Myf5Cre-Pcyt2* mice (Extended Data Figure 7G-J). Moreover, we crossed *Pcyt2*$^{flox/flox}$ mice to the *AdipoQCre* line to remove *Pcyt2* specifically in white and brown adipose tissue[23] and did not observe any differences in growth, blood glucose, nor any apparent pathologies (Extended Data Figure 8A-C). Tissue-specific deletion of *Pcyt2* in motor neurons (*Mnx1Cre*; Extended Data Figure 8D-F), gut epithelium (*Villin1Cre*; Extended Data Figure 8G-I), and mammary and skin epithelial cells (*K14Cre*, Extended Data Figure 8J-L), neither resulted in apparent developmental nor degenerative deffects up to 12 months of age. This lack of apparent phenotypes in the above tested Cre-deleter mouse lines suggests that Pcyt2 does not play an essential developmental role in these tissues[24–30].

To further explore muscle-specific deletion of Pcyt2, we crossed *Pcyt2*$^{flox/flox}$ with *Mck-Cre* mice. *MckCre-Pcyt2* mice have been reported with a beneficial effect at young age[31], which is in contrast to our findings in *Myf5Cre-Pcyt2* mice and *PCYT2* mutant patients. Critical membrane myotome development is established early in utero, facilitated by addition and fusion of muscle satellite cells (MSC) and adult myoblasts. Perturbations in these early events manifest as rapid onset and severe dystrophies[32,33]. Given that McKCre is active late in muscle formation (peak Cre activity at P10), and in mature muscle without activity in early myotome, MSCs and myoblasts[34,35 32,33], this coupled with slow membrane PE turnover[36] might explain observed phenotypical differences. Importantly, whereas young *MckCre-Pcyt2* mice up to 4 months of age did not display degenerative phenotypes[31], older *MckCre-Pcyt2* mice displayed muscle weakness with a late onset at 18 months of age (Extended Data Figure 8M,N).

Pcyt2 muscle deficiency alters mitochondrial function

Given that phosphatidylethanolamines are abundant in cell but also mitochondrial membranes[37], we analyzed if *Pcyt2* deficiency affects mitochondrial homeostasis. Parallel to whole tissue lipidome changes, there was also a significant reduction of PE species in muscle mitochondria from *Myf5Cre-Pcyt2* mice (Figure 4A,B). Global RNA transcriptome analyses of muscle from 10-day old control and *Myf5Cre-Pcyt2* mice revealed enrichment of genes associated with mitochondrial dysfunction (Figure 4C). Interestingly, when we analyzed skeletal muscle mitochondrial activity from 2 months old *Myf5Cre-Pcyt2* mice, we observed an increase in activity, followed by a drop in the activity from 6 months old *Myf5Cre-Pcyt2* mice (Figure 4D; Extended Data Figure 9A-C). Further, we observed an increase in mitochondrial ROS in the isolated myofibers, as well as increased levels of antioxidant catalase activity and protein oxidative damage in the skeletal muscle of 6 months old Myf5Cre-Pcyt2 mice (Figure 4E-G). As expected, markers of cellular stress (pJNK, Foxo1) and muscle wasting (Atrogin, MuRF1, Fbx031) were increased in the muscles of 6 months old *Myf5Cre-Pcyt2* mice (Figure 4H,I). The ultrastructural morphology and contents of mitochondria appeared unchanged in muscles even in adult mutant mice with apparent phenotype (Extended Data Figure 9D,E). Thus, increased cellular stress including energy stress, ROS mediated protein damage, and unbalanced proteostasis accelerate muscle degeneration in *Myf5Cre-Pcyt2* mice.

Next, we tested if the accumulation of the Pcyt2 substrate phosphoethanolamine, was affecting the mitochondria. Compared to control mitochondria, there was no additive, inhibitory effect of phosphoethenolamine on the activity of skeletal muscle mitochondria isolated from *Myf5Cre-Pcyt2* mice (Extended Data Figure 9F), suggesting that intra-mitochondrial overaccumulation of phosphoethanolamine is not responsible for the observed reduction in activity of skeletal muscle mitochondria from *Myf5Cre-Pcyt2* mice.

Given that we observed impaired skeletal muscle mitochondrial activity, we attempted to improve the pathological features of *Myf5Cre-Pcyt2* mice by administering mitochondria-targeted antioxidant SS-31 daily for two months, starting from 4 months of age. Although there was a mild improvement in the grip strength and tissue weight, the effect was not significant (Extended Data Figure 9G,H).

We also tested a potential role of Pcyt2 and Pcyt2-derived PE in sarcolemmal Ca^{2+} handling and autophagy. We failed to observe any structural changes or alterations in Ca^{2+} release and Ca^{2+} uptake in isolated myofibers from 6-month-old *Myf5Cre-Pcyt2* mice manifesting gross phenotypes (Extended Data Figure 10 A-C), suggesting that sarcoplasmic reticulum Ca^{2+} handling was preserved. PE conjugation to ATG8 is also necessary for autophagy[38]. However, PE-ATG8 conjugation was comparable in both quadriceps and diaphragm muscles of 6-month-old control and *Myf5Cre-Pcyt2* mice under both fed and fasted conditions, without evident accumulation of p62/SQSTM1 under fed or fasting conditions (Extended Data Figure 10 D-I). Of note, it has been previously shown that genetic inactivation of Atg7 and LC3 PE lipidation in Myf5-derived lineages induces brown fat over-activation, but does not lead to muscle weakness, degeneration, not muscle dystrophy[39], contrasting with our *Myf5Cre-Pcyt2* mice. Taken together, loss of Pcyt2 does not affect PE-modifications in autophagy or sarcoplasmic reticulum but affects mitochondrial function. However, given that mitochondria targeted therapy didn't rescue the muscle weakness of Myf5Cre-Pcyt2 mice, this suggested that there are additional cellular defects driving the observed pathology due to Pcyt2 deficiency.

Pcyt2 deficiency affects sarcolemmal lipid bilayer physicochemical properties

Impaired sarcolemmal stability causes myofiber degeneration in muscular dystrophies[40]**.** Our muscle whole tissue lipidomics data showed a significant decrease in PEs containing long chain fatty acids (FAs)(Figure 1J,K), which are abundant membrane lipids[37]**.** Therefore, we

hypothesized that the reduced abundance of PEs containing long chain FAs in *Myf5Cre-Pcyt2* mice might also affect formation and stability of the sarcolemmal lipid bilayer, driving the muscular pathology. To test this hypothesis, we first evaluated whether the organization of the sarcolemmal lipid bilayer was altered in *Myf5Cre-Pcyt2* mice. Spectral imaging of NR12S-stained giant plasma membrane vesicles (GPMVs) provides structural information of lipid bilayers in their native compositional complexity and structural organization[41]. We derived the parameter of general polarization (GP), with higher values corresponding to tightly packed, rigid lipid bilayer and lower values corresponding to loosely packed, soft bilayer. Strikingly, polarization microscopy of GPMVs derived from *Myf5Cre-Pcyt2* myoblasts displayed loosely packed and softer lipid bilayer as compared to control myoblasts-derived GMPVs (Figure 5A,B). To further address if the membrane bilayer changes persist in the myofibers, we assessed GPMVs from myofibers immediately after isolation from the tissue (Figure 5C). GPMVs isolated from myofibers of *Myf5Cre-Pcyt2* mice again showed significant reduction of lipid packing and soft lipid bilayer (Figure 5D).

To directly address how these structural-chemical changes of the membrane lipid bilayer affect mechanical properties, we employed high-resolution Brillouin Light Scattering Microscopy (BLSM) on isolated myofibers[42]. Scans using BLSM revealed a significant reduction in the surface stiffness of myofibers isolated from *Myf5Cre-Pcyt2* mice compared to controls (Figure 5E,F). Atomic force microscopy on single myofibers further confirmed that *Myf5Cre-Pcyt2* myofibers have a higher degree of membrane deformity after applying pressure at a nanoscale level and reduced membrane stiffness compared to *Pcyt2*-expressing muscle cells (Figure 5G,H). Thus, loss of *Pcyt2* in myoblasts and myofibers results in an altered architecture of membrane lipid bilayers, directly perturbing sarcolemmal lipid bilayer mechanical properties of rigidity and stiffness.

Pcyt2 deficiency impairs sarcolemmal stability

An intact cell membrane architecture is critical for membrane barrier function. The sarcolemma undergoes recurrent injury via contraction mediated-mechanical strain and needs structural stability for proficient skeletal muscle function[43]. To determine if the perturbed architecture of the sarcolemma in *Myf5Cre-Pcyt2* mice leads to altered permeability, we injected 6-month-old control and *Myf5Cre-Pcyt2* mice intraperitoneally with

Evans blue (<1kDA)[44]. We observed an extensive accumulation of Evans blue in the quadricep muscles of *Myf5Cre-Pcyt2* mice relative to controls (Figure 6A,B). To further explore sarcolemmal stability, we induced laser mediated membrane microinjury on freshly isolated myofibers and quantified the extent of damage in real time, by measuring intracellular influx of the fluorescent fm1-43 dye[45]. Following laser microinjury, Control myofibers displayed minimal influx of fm1-43, whereas *Myf5Cre-Pcyt2* myofibers showed increased permeability to the dye (Figure 6C; Video S1-S4).

To directly address sarcolemmal durability to strain *in vivo*, we subjected control and *Myf5Cre-Pcyt2* mice to eccentric exercise regime. Eccentric exercise is a potent inducer of sarcolemma strain, while having very low energy requirement compared to concentric exercise of the same load[46]. During the early acclimatization phase (low speed downhill running; 4 meters min^{-1} for 40 min) and the intermediate phase (4 meters min^{-1} for 40 min plus 9 meters min^{-1} for 20 minutes) of the exercise, *Myf5Cre-Pcyt2* mice performed similarly to their littermates (Figure 6D). However, during the late stress phase (20 meters min^{-1} for 20 minutes), *Myf5Cre-Pcyt2* mice failed to complete the exercise (Figure 6D; Video S5). We analyzed the skeletal muscle after the last phase of training. The weights of the quadricep and gastrocnemius muscles were higher after training in control mice while the muscles of *Myf5Cre-Pcyt2* mice failed to undergo hypertrophy (Supplementary Figure 7A); instead, their skeletal muscles exhibited apparent muscle damage with foci of inflammation, fat cell deposits and fibrosis (Figure 6E-F, Supplementary Figure 7B). In parallel, we observed a significant increase in blood muscle creatine levels after exercise (Figure 6G). Dysferlin, a sarcolemma associated membrane repair, was aberrantly localized in *Myf5Cre-Pcyt2* quadricep muscles after training (Supplementary Figure 7D). In addition, we observed disorganized F-actin networks in *Myf5Cre-Pcyt2* mice after training (Figure 6H). Of note, the number of $Pax7^+$ progenitors in the skeletal muscle appeared similar between trained control and *Myf5Cre-Pcyt2* mice (Supplementary Figure 7E). Thus, Pcyt2 PE synthesis is required for sarcolemmal stability, preventing muscle damage and hypertrophy during eccentric exercise.

Muscle-specific *Pcyt2* gene therapy ameliorates muscle weakness in mutant mice

Currently, there is no treatment for the disease caused by *PCYT*2 deficiency. Since gene therapies made significant advances in the treatment of rare diseases, we sought to therapeutically ameliorate the muscle weakness *Myf5Cre-Pcyt2* mice. We cloned Pcyt2 under the control of the muscle creatine kinase 8 (CK8) promoter/enhancer into AAV6 vector cassete[47,48]. The *CK8:Pcyt2-HA* vector-carrying AAV6 viral particles were injected into 4 day old *Myf5Cre-Pcyt2* mice and the muscles of these mice were assessed 6 months after the treatment (Figure 7A). This approach resulted in Pcyt2-HA protein overexpression and increased PE levels in the skeletal muscles of *Myf5Cre-Pcyt2 AAV6:CK8:Pcyt2-HA* injected mice compared to untreated *Myf5Cre-Pcyt2* controls (Figure 7B,C, Supplementary Figure 8A).

Strikingly, the *AAV6:CK8:Pcyt2-HA* treated mutant mice displayed a significant increase in grip strength, increased skeletal muscle mass and myofiber diameter (Figure 7D-F; Supplementary Figure 8B). Moreover, skeletal muscles from *Myf5Cre-Pcyt2 AAV6:CK8:Pcyt2-HA* injected mice, displayed improved muscle membrane parameters (Figure 7G,H) and improved mitochondrial respiration (Figure 7I).

Muscle-specific *Pcyt2* gene therapy improves muscle health in aging

Progressive muscle atrophy is a critical determinant of frailty in aging. Muscle aging is commonly associated with diminished membrane integrity, increased susceptibility to damage, and diminished repair after exercise[49–51]. As *Myf5Cre-Pcyt2* mice displayed degenerative features that are also found in aging muscles, we assessed a potential role of *Pcyt2* in muscle aging. Indeed, Pcyt2 mRNA expression and enzymatic activity in quadricep muscle were reduced in aged, pre-sarcopenic mice compared to young mice (Figure 8A, Supplementary Figure 8C). Importantly, PCYT2 activity and levels were substantially decreased in quadricep muscle biopsies of otherwise healthy 45-62 year-old compared to 20-30 year-old humans (Figure 8B, Supplementary Figure 8D,E). Thus, in mice and humans, Pcyt2 expression and even more activity, decline with aging. Accoupling this, we found that in the muscles of aged, pre-sarcopenic mice, some of the most significantly affected lipids were PE species (Figure 8C). To test whether increasing the levels of Pcyt2 can improve muscle function in aged mice, we aimed to rejuvenate aged muscles via overexpression of *Pcyt2*. *AAV6:CK8:Pcyt2-HA* or saline (as control) were injected retro-orbitally into 24 month-old male C57B6/J mice (Figure 8D). and the expression of Pcyt2-HA and increase of total muscle PE

levels in the quadricep muscle was confirmed after 2 months (Figure 8E,F; Supplementary Figure 8F).

Using our newly established microscopy-based analysis pipeline, we addressed whether the observed *AAV6:CK8:Pcyt2-HA* dependent increase of PE lipids in the muscles of aged mice would also reflect on myofiber membrane physical parameters. Indeed, there was a significant increase in muscle membrane stiffness as measured by both polarization microscopy and Brillouin spectroscopy (Figure 8G,H). Moreover, the bioenergetics of the muscle showed beneficial changes, with improved mitochondrial capacity and respiratory control ratio, a measure of ATP production efficiency (Figure 8I, Supplementary Figure 8G). Accompanying this, there was a significant increase in the myofiber diameter of *AAV6:CK8:Pcyt2-HA* mice compared to control mice 2 months after gene delivery (Figure 8J). Remarkably, we observed significantly improved grip strength at 1 and 2 months after gene delivery in *AAV6:CK8:Pcyt2-HA* mice compared to control mice (Figure 8K, Supplementary Figure 8H).

Discussion

In summary, our results uncover a critical and conserved role for Pcyt2 and Pcyt2-regulated lipid biosynthesis. We show that loss of Pcyt2-dependent lipid biosynthesis causes a previously unrealized form of muscular dystrophy, characterized by an aberrant muscle development, progressive muscle weakness and wasting, failure to thrive and shortened lifespan. Our work reveals that with *Pcyt2* deficiency, reduction of long chain PE synthesis compromises the sarcolemma lipid bilayer stability, as well as myofiber mitochondria homeostasis. Given that PEs are predominantly membrane lipids, we infer that Pcyt2-dependent PE synthesis is essential for the lipid bilayer of sarcolemma and PE enriched membranes of mitochondria.

This form of muscular dystrophy is very rare, in that a lipid species provides mechanical support to cellular membranes, as opposed to other forms of dystrophies that are caused by aberrations of cytoskeletal, mitochondrial or extracellular proteins[52], and may thus also have distinct therapeutic implications. Whereas muscular dystrophy is typically caused by the

disruption of proteins that support the sarcolemma, we show that loss of *Pcyt2* leads to intrinsic changes of the membrane lipid bilayer, thus representing a unique disease mechanism.

Besides being essential to sarcolemmal lipid bilayer composition and stability, PE lipids are also abundant in the inner mitochondrial membrane. Although majority of mitochondrial PEs are derived via decarboxylation of phosphatidylserine inside the mitochondria[53], the observed mitochondrial dysfunction with increased generation of mtROS in myofibers of Myf5Cre-Pcyt2 mice clearly demonstrate that Pcyt2-dependent PE synthesis is additionally important in generating mitochondrial PE lipids. Decreased mitochondrial membrane viscosity coupled with impaired mitochondrial activity was already observed in degenerative diseases [54], while decreased membrane viscosity increases ROS diffusion across the bilayer [55,56]. This phenomenon could explain alterations of mitochondrial respiration as well as increase in ROS levels in myofibers which coupled with sarcolemmal instability, triggers muscle mitochondrial functional decline, myofiber stress, increased ROS levels, oxidative protein damage and activation of the JNK-FoxO1 axis of muscle atrophy in Myf5Cre-Pcyt2 mice. Consequently, these perturbations result in dramatic muscle degeneration, progressing to a severe dystrophy with inflammation and shortening of lifespan. Intriguingly, we and others[31] have observed an initial increase of mitochondrial activity in Pcyt2 deficient muscles, without an increase in total mitochondrial numbers. This initial response most likely represents a compensatory response typical of mitochondrial diseases[57].

Mouse models that initiate gene loss very early in myotome development, faithfully recapitulate human muscular dystrophies in many pathological features including stunted growth and progressive muscle degeneration with shortened lifespan[32,33,52]**.** MckCre-Pcyt2 deficient mice did not display muscular weakness at an early adulthood [31], and we observed muscle weakness in old (20 months old) MckCre-Pcyt2 mice. Mck promoter drives Cre expression late in the muscle development (peak activity P10)[34]. However, critical muscle membrane organization occurs very early in the developing myotome[52]. Thus, relatively later Cre activation driven by the *Mck* promoter would miss this critical developmental stage, which is not the case for inherited, disease-causing mutations in humans. Moreover, given that MckCre activity is restricted to mature muscles[34,35], this bypasses the muscle stem cell pool rendering them “wild type”, which can then actively repopulate and repair the Pcyt2

deficient muscle, and delay muscle degeneration. This phenomena of dependence of disease severity on the timing of the gene disruption was already observed for several animal models of membrane-related human dystrophies, where only mouse mutants with early gene deletion faithfully recapitulated patient phenotypes[32,33]. Our findings in zebrafish model, mouse mutant and aged models, as well as in rare disease patients with weakness and muscle wasting [58] support that the Pcyt2-dependent Kennedy pathway is essential for muscle health.

As seen in rare disease patients, failure to thrive preceded the apparent progressive weakness and degeneration in Myf5Cre-Pcyt2 mice. Muscle growth by myoblast fusion and hypertrophy is essential for both muscle and whole-body size [59]. Both mechanisms of muscle growth were affected in Myf5Cre-Pcyt2 mice. Apart from being important membrane building blocks, phosphatidylethanolamines are important in modulating membrane physicochemical properties[4]. Due to their relatively small polar head group and consequently a conical shape[4], phosphatidylethanolamines form a negative membrane curvature required for membrane bending during the cell fusion process[60]. Therefore, any genetic insufficiency of phosphatidylethanolamines would negatively affect the efficiency of both membrane neo-genesis during tissue growth and cellular fusion, affecting tissue growth. However, solely stunted growth or impaired myoblast fusion wouldn't necessarily result in degenerative phenotypes later in adulthood [61–64].

Our findings indicate that the muscle tissue is especially vulnerable to loss of Pcyt2 and Pcyt2 synthesized PE. It is well established that distinct tissues have a diverse membrane lipid composition[4] and may be differentially dependent on Pcyt2. Indeed, mining the Achilles Depmap data portal, which contains gene essentiality scores from 769 cell lines[65], we found that Pcyt2 is not essential for a large majority of the tested cell lines (4.8% dependent cell lines). For comparison, many more cell lines (54% dependent cell lines) are dependent on choline-phosphate cytidylyltransferase (Pcyt1a), a bottleneck enzyme for synthesis of phosphatidylcholines in the parallel branch of the Kennedy pathway. The muscle dependency on Pcyt2 derived PE might be explained by the general chemical properties of PE lipids. Increasing PE concentrations increase the viscosity of the liposomes[66], therefore we hypothesize that the constant mechanical strain and contraction of the myofibers render muscle membranes dependent on PE for mechanical support. The essential dependency of myofibers on Pcyt2 derived PE compared to other cell types, is supported by our findings from

various tissue-specific mutants, as well on BAT functionality in Myf5Cre-Pcyt2 mutants. Moreover, current pathophysiological symptoms in the rare disease patients are mainly restricted to growth and neuromuscular parameters, with no other reported physiological defects such as core body temperature maintenance. This indicates that other cell types are able to engage alternative molecular mechanisms to compensate for the deficiency in Pcyt2-dependent PE synthesis. Future research should illuminate which synthesis or lipid uptake mechanisms from periphery are responsible for this. Interestingly, inherited mutation in choline kinase beta (Chkb) results in loss of synthesis of another membrane lipid, phosphocholine and consequently phosphatydilcholine, causing neuronal pathology as well as muscular dystrophy without affecting other tissues[67,68], thus resembling certain pathological features of inherited PCYT2 mutations. It is intriguing that nervous and muscle tissue are particularly vulnerable to deficiency of certain membrane lipids as opposed to other cell types stimulating a wider field of research on cell type-specific changes in cell membrane lipid composition and lipid bilayer physicochemical parameters in various biological processes and pathological conditions.

It is important to note that humans the effect of the mutations in either EPT1 or PCYT2 vary between affected individuals (Supplementary Figure 1, Supplementary Figure 2). In some patients where the muscle parameters were addressed the effect on muscle strength was apparent with weakness and muscle wasting while other patients showed no signs of reduced muscle strength[58]. Muscle biopsy on one clinical case confirmed the reduction in muscle fiber size[69]. Gross muscle strength evaluation revealed that all of our reported EPT1 and PCYT2 mutation patients have muscle weakness. This variation in muscle strength parameters might be explained by the effects of the different mutations on the EPT1 and PCYT2 enzymatic activity resulting in pathogenic thresholds of PE concentrations. A future comparative study of all reported individuals, including detailed characterization of muscle biopsies and determination of enzymatic activities of EPT1 and PCYT2, should provide further insights on the severity of the muscle phenotypes in these patients in regard to the corresponding enzymatic efficiency.

Muscle atrophy is a hallmark of aging, and a leading cause of frailty and dependency. We found that Pcyt2 levels and activity markedly declined in muscles from aged rodents and humans. Decreased expression of Pcyt2 mRNA was recently observed in aged rat muscles[70].

It is possible that this reduction occurs as a consequence of a metabolic switch in aged muscle, which in aging appears to be more directed towards triglyceride and cholesterol synthesis[71]. Indeed, low density lipoprotein, cholesterol oxysterols or LXR (liver X receptor, a transcriptional regulator of cholesterol, fatty acid, and glucose homeostasis) inhibit Pcyt2 [72]. Importantly, our data show that PCYT2 enzymatic activity are significantly reduced in aged muscles, with long chain PE membrane lipids being one of the most significantly reduced lipid species in aged muscles. Moreover, we found that increasing Pcyt2 expression in aged mice improves several parameters of aged myofibers through increasing tissue PE lipid levels, ameliorating muscle strength decline. Taken all this together, Pcyt2 upregulation could be considered as a potential treatment to improve muscle frailty.

Acknowledgements

The authors would like to thank the patients and their families for participating in the study. We would like to thank all members of our laboratories for helpful discussions, Angela Anderson and Life Science Editors for editorial support. We are grateful to Vienna Biocenter Core Facilities: Mouse Phenotyping unit, Histopathology unit, Bioinformatics unit, Biooptics unit, Electron microscopy unit and Comparative medicine unit. We are grateful to the Lipidomics facility and K. Klavins T. Hannich at the CeMM Research Center for Molecular Medicine of the Austrian Academy of Sciences for assistance with lipidomics analysis. We would also like to thank to Tao Huan and Alyssa Hui (UBC Vancouver, Canada) for mouse tissue and mitochondria lipidomics analysis. We thank A. Klymchenko (Laboratoire de Bioimagerie et Pathologies Université de Strasbourg, Strasbourg, France) for providing the NR12S probe. We are thankful to the Sen. Paul D. Wellstone Muscular Dystrophy Cooperative Specialized Research Center Viral Vector Core facility (Seattle, US) for AAV6 production. We would also like to thank Kevin P Campbell and Mary E Anderson (University of Iowa, Carver College of Medicine, Iowa US) for advice on muscle tissue handling. We would also like to thank Ahmed Al-Qassabi from the Sultan Qaboos Universit y for the clinical assessment of the patients. D.C and J.M.P. are supported by the Austrian Federal Ministry of Education, Science and Research, the Austrian Academy of Sciences, and the City of Vienna, and grants from the Austrian Science Fund (FWF) Wittgenstein award (Z 271-B19), the T. von Zastrow Foundation, and a Canada 150 Research Chairs Program (F18-01336). J.S.C. is supported by grants RO1AR44533 & P50AR065139 from the US National Institutes of Health. C.K. is supported by a grant from the Agence Nationale de la Recherche (ANR) (ANR-18-CE14-0007-01). A.V.K. is supported by European Union'sHorizon 2020 research and innovation programme under theMarie Skłodowska-Curie grant agreement No 67544, an Austrian Science Fund (FWF) No P-33799, AW is supported by Austrian Research Promotion Agency (FFG) project No 867674. E.S. is supported by a SciLifeLab fellowship and Karolinska Institutet Foundation Grants. Work in the GSF laboratory is supported by the Austrian Academy of Sciences, the European Research Council (ERC AdG 695214 GameofGates) and the Innovative Medicines Initiative 2 Joint Undertaking (grant agreement No 777372, ReSOLUTE). SB, ML and RY acknowledge the support of the Spastic Paraplegia Foundation.

Author Contributions

D.C. together with J.M.P. designed and supervised the mouse study and wrote the manuscript with the input from the co-authors. All experiments were performed and established by D.C. with the following exceptions: K.E. performed Brillouin light scattering microscopy measurements. E.S. performed GPMVs isolation and image analysis with assistance from D.C. E.K. performed synergic ablation assay and analysis under supervision form Z.R. T.F. performed treadmill experiment with assistance from D.C. and under supervision from Z.R. R.Y. collected and analyzed zebrafish models under supervision from M.L. L.X.H. and V.S. performed lipidomics analysis under supervision of G.S.-F. A.T. and S.G. performed Pcyt2 enzyme activity analysis under supervision of M.B. A.A. performed *in vivo* brown fat activity and Ucp1 RT-PCR analysis under supervision from Cl.K. A.W. performed respiration analysis under supervision from A.Ko. M.O. performed and analyzed mouse calorimetry experiments. Ca.K. and C.S. performed myofiber calcium kinetics experiment, with analysis and supervision under V.J. S.J.F.C. assisted with western blot experiments. M.N. performed bioinformatic analysis of RNA sequencing and of efficiency of Pcyt2 deletion in mice. A.Ka. performed myositis scoring. N.D.M. performed atomic force microscopy measurements and data analysis with assistance from D.C. T.S. and B.H. assisted in histological analysis. L.H. performed AAV6 i.v. injections. A.H. assisted in tissue sampling for western blot experiments. S.J. provided *Pcyt2* floxed mice. E.R. and T.G. collected human muscle biopsies. J.S.C. generated AAV6 vector and provided guidance with all AAV experiments. J.M., F.A.-M. and S.B. identified PCYT2 human mutant carriers, collected growth data and generated growth curves.

Ethics statement

Declaration of Interests

The authors declare no competing interests.

Figure legends

Figure 1. Phenotypes of human *PCYT2* rare disease mutations and *pcyt2* mutant zebrafish.

(A) Body weight and **(B)** height gain of patient (male) carrying the homozygous nonsense variant 3c.1129C>T (p.Arg377Ter) in the *PCYT2* gene. Controls indicate WHO standards of median weights and heights at the respective ages +/- 2 standard deviations (SD). **(C)** Representative appearance and quantifications of body length of control and hypomorphic *pcyt2* mutant zebrafish at 14 months post fertilization. n=4 for each group. **(D)** Representative muscle sections and muscle myofiber sizes of control (n=4 animals and 233 myofibers in total) and hypomorphic pcyt2 (n=4 animals and 233 myofibers in total) zebrafish. Scale bar 50µm. Myofibers of the same anatomical region were analyzed with ≥ 50 myofibers per animal **(E)** Body weight gains of control (n=15) and *Myf5Cre-Pcyt2* (n=11) littermates on standard chow diet. Two-Way ANOVA with multiple comparison followed by Bonferroni correction was used. ****$p^{(genotype)} < 0.0001$ **(F)** Appearance of 4 days old (P4) and 56 days old (P56) control and *Myf5Cre-Pcyt2* littermates. Scale bars are 1 cm for P4 and 2 cm for P56. **(G)** Skeletal muscle appearance (quadriceps) isolated from 10 days control and *Myf5Cre-Pcyt2* littermate mice. **(H)** Representative cross sections and **(I)** skeletal muscle myofiber diameter sizes from 6 months old control (n=4 mice and 570 myofibers) and *Myf5Cre-Pcyt2* mice (n=4 mice and 640 myofibers). Myofibers were imaged using 10X magnification with ≥ 100myofibers analyzed per mouse. Scale bar 100µm**. (I)** Lipidomics analyses from quadriceps muscles isolated from 10 days old *Myf5Cre-Pcyt2* and littermate control mice. Data are shown relative to control values. CE-cholesterol ester; Cer-Ceramides; DAG-diacylglycerols; LPC-lysophosphatidylcholines; LPE-lysophosphatidylethanolamines; PC-phosphatidylcholines; PE-phosphatidylethanolamines; PG-phosphatidylglycerols; PI-phosphatidylinositols; PS-phosphatidylserines; SM-sphingomyelins; TAG-triacylglycerols. n=4 per group. **(J)** Detailed analysis of PE species with different chain lengths from quadriceps muscles of *Myf5Cre-Pcyt2* as compared to control mice.

598 Data are shown as means ± SEM. *p < 0.05, **p < 0.01, ***p < 0.001, and ****p < 0.0001,
599 n.s. not significant. Unpaired Student t-test with Welch correction was used for statistical
600 analysis unless stated otherwise.

601

602 **Figure 2. *Pcyt2* deficiency affects muscle stem cell fusion and muscle**
603 **hypertrophic growth.**

604 **(A)** Representative images of Mf20 stained myofibers and **(B)** primary myoblast fusion index
605 quantification of Control and *Myf5Cre-Pcyt2* primary myoblasts after differentiation *in vitro*.
606 Nine biological replicate myoblast cultures from three independent isolations were used.
607 Each dot represents a calculated fusion index from in total n=9 cultures for each group. ≥ 300
608 nuclei were counted per one culture. Myofibers were imaged using 10X magnification. Scale
609 bar 50µm**. (C)** Representative images and myofiber diameter quantification of Control (n=145
610 myofibers) and *Myf5Cre-Pcyt2* (n=158 myofibers) after differentiation from primary
611 myoblasts *in vitro*. Myofibers were imaged using 10X magnification. Scale bar 50µm **(D)** RT-
612 PCR analysis of fusion and differentiation markers of Control and Myf5Cre-Pcyt2 myoblasts
613 after 48h in differentiation media. N=5 cell cultures from 5 different animals per group. **(E)**
614 Representative images and myoblast fusion index quantification of primary myoblasts with
615 addition of vehicle (DMSO) and SA-Ro phosphatidylethanolamine binding peptide in
616 differentiation media. Nine biological replicate myoblast cultures from three independent
617 isolations were used. Each dot represents a calculated fusion index from in total n=9 cultures
618 for each group. ≥ 300 nuclei were counted per one culture. Myofibers were imaged using 10X
619 magnification. Scale bar 50µm**. (F)** Hypertrophic muscle growth in control and Myf5Cre-Pcyt2
620 mice. Following synergic ablation or sham surgery, M. plantaris weights were determined on
621 the compensating limb. Each dot represents individual mice.

622 Data are shown as means ± SEM. *p < 0.05, **p < 0.01, ***p < 0.001, and ****p < 0.0001,
623 n.s. not significant. Unpaired Student t-test with Welch correction was used for statistical
624 analysis unless stated otherwise.

625

Figure 3. Inactivation of *Pcyt2* in mice leads to progressive weakness, muscle atrophy, inflammation and accelerated ageing.

(A) Representative images of 6 months old control and *Myf5Cre-Pcyt2* male mice and (B) quantification of progressive worsening of hind limb clasping **(B)**. Each dot represents one mouse, values are average of three measurements per mouse; scale bar 1 cm. **(C)** Age-dependent decline in grip strength in male control and *Myf5Cre-Pcyt2* littermates. Each dot represents one mouse, values are average of three measurements per mouse. **(D)** Typical kyphosis appearance and kyphosis severity in 8 months old control (n=4) and *Myf5Cre-Pcyt2* male mice (n=7). **(E)** Evident scoliosis (arrows) in a patient carrying the homozygous nonsense variant NM_001184917.2:3c.1129C>T (p.Arg377Ter) in *PCYT2*. **(F)** Representative image and quantification of relative muscle mass changes of 12 months old versus 6 months old control and *Myf5Cre-Pcyt2* male littermates. QA, quadriceps; GC, gastrocnemius; TA, tibialis anterior muscles. Scale bar = 1 cm; n=7 per group. **(G)** Quantification of myofibers with central nuclei in quadriceps muscles from 8 months old control and *Myf5Cre-Pcyt2* male mice. n=3 mice per group. Scale bar 100μm. **(H)** Muscle inflammation as determined by H&E staining. Data are from 12 months old male mice. Data are representative for n=4 mice per group. Scale bar 100μm. **(I)** Representative cross section of tibial bone in 12 months old control and *Myf5Cre-Pcyt2* male mice with quantification of tibial bone cortical thickness. Randomly assigned 5 areas from n=4 mice per group were quantified. Scale bar 100μm. **(J)** Survival curves for control and *Myf5Cre-Pcyt2* male mice. n=22 mice per group. For statistical analysis Mantel Cox test).

Data are shown as means ± SEM. Each dot represents data point from individual mice unless stated otherwise. *$p < 0.05$, **$p < 0.01$, ***$p < 0.001$, and ****$p < 0.0001$, n.s. not significant Unpaired Student t-test with Welch correction was used for statistical analysis unless stated otherwise.

Figure 4. *Pcyt2* deficiency severely affects muscle mitochondrial homeostasis as opposed to brown fat mitochondria.

(A) Total PE levels and **(B)** global lipidomics analyses of purified mitochondria isolated from 2 months old Control and *Myf5Cre-Pcyt2* male mice. N=6 mice per group **(C)** Pathway enrichment analysis of differentially expressed genes in Control and Myf5Cre-Pcyt2 quadriceps isolated from 10 days old male pups. Evident enrichment of mitochondrial dysfunction linked genes specifically in the muscle of Myf5Cre-Pcyt2 mice. N=4 mice per group. **(D)** Muscle mitochondrial function assessed by measurements of complex I linked activity on isolated mitochondria from 2 months and 6 months old control and *Myf5Cre-Pcyt2* male mice respectively. Paired Student t-test. **(E)** Measurement and quantification of myofiber mitochondrial reactive oxygen species (mtROS) in isolated myofibers (EDL muscle) from 6 months old male control (n=3 mice and 61 myofiber) and *Myf5Cre-Pcyt2* mice (n=3 mice and 59 myofibers) as detected by MitoSox staining. Each dot represents relative amount of mtROS from a single myofiber. Scale bar 25µm. **(F)** Evidence of increased protein oxidative damage in quadriceps muscles isolated from 6 months old male *Myf5Cre-Pcy*t2 mice. Representative blots are shown for n=3 mice per group. **(G)** Catalase anti-oxidant activity in quadriceps muscles from 6 months old control and *Myf5Cre-Pcyt2* male mice**. (H)** Increased levels of phospho-JNK (pJNK) and FoxO1 in quadriceps muscles from 6 months old male *Myf5Cre-Pcyt2* mice (n=3) as compared to controls (n=3). 4 animals per group were analyzed in total, representative blot from 3 animals per group is shown **(I)** Increased levels of myofiber wasting markers in muscles of 8 months old male *Myf5Cre-Pcyt2* mice**.**

Data are shown as means ± SEM. Each dot represents data point from individual mice unless stated otherwise. *$p < 0.05$, **$p < 0.01$, ***$p < 0.001$, and ****$p < 0.0001$, n.s. not significant. Unpaired Student t-test with Welch correction was used for statistical analysis unless stated otherwise.

Figure 5. Loss of *Pcyt2* results in altered muscle membrane architectures.

(A) Scheme of GPMV isolation from primary myoblasts. **(B)** Polarization microscopy analysis of NR12S dye-stained myoblast-derived GPMVs from male control (n=71) and *Myf5Cre-Pcyt2*

(n=71) myoblasts. Each dot represents GP values of a single GPMV. GPMVs were derived from two independent isolations Scale bar 10μm. **(C)** Scheme and representative example of GPMVs (arrows) immediately after isolation from skeletal myofibers**.** Images are taken at 0 and 30 minutes under GPMV conditions. Scale bar 50μm. **(D)** Polarization microscopy of NR12S-stained GPMVs from control (n=58) and *Myf5Cre-Pcyt2* (n=99) from primary myofibers (as shown in **C**). from two independent isolations. Representative images and quantifications are shown. Each dot represents GP values of a single GPMV. Scale bar 10μm. **(E)** Scheme of Brillouin light scattering microscopy for freshly isolated myofibers. **(F)** Surface stiffness analysis measured by Brillouin frequency shift (BFS) from isolated myofibers for male control (n=3 mice and 60 myofibers in total) and *Myf5Cre-Pcyt*2 (n=3 mice and 60 myofibers in total). Left panels indicate representative Brillouin images. Each data point in the right panel represents a BFS peak value of the individual myofiber surface. **(G)** Representative qualitative membrane stiffness data of male control and *Myf5Cre-Pcyt2* myofibers assessed by atomic force microscopy. Displayed by curve angles in the approach (0 to -1000nm) and retraction phase (-1000 to 0nm), the cantilever bends less for *Myf5Cre-Pcyt2* myofibers, indicating lower surface stiffness. In the prolonged part of retraction phase (0 to 400nm) the cantilever remains deeper within the *Myf5Cre-Pcyt2* myofibers, indicating higher degree of surface deformity upon pressure. **(H)** Quantitative myofiber membrane stiffness as assessed by atomic force microscopy (Young's modulus scale in kilopascal, kPa). For each myofiber we collected ≥4000 measurements (5μm X 5μm area). Matlab's Randsample function was used to uniformly sample each myofiber measurements. Each dot represents 500 data points per each myofiber, from control (n=20) and *Myf5Cre-Pcyt2* (n=26) myofibers. Data are shown as means ± SEM.

Data are shown as means ± SEM. *$p < 0.05$, **$p < 0.01$, ***$p < 0.001$, and ****$p < 0.0001$, n.s. not significant. Unpaired Student t-test with Welch correction was used for statistical analysis unless stated otherwise.

Figure 6. Pcyt2 is essential for muscle membrane integrity and strain tolerance.

(A) Penetrance of Evans blue into the quadriceps muscle of 6 months old male control and *Myf5Cre-Pcyt2* mice after i.p. injection. Gross morphologies and histological sections are

shown. Scale bars are 1cm and 100µm. **(B)** Quantification of Evans blue after extraction from the muscle. n=3 per group. **(C)** Laser induced damage of isolated myofibers from male 6 months old control (n=9) and *Myf5Cre-Pcyt2* (n=12) myofibers. The injured membrane areas of the myofibers are indicated by arrows. Right panel shows quantification of fm43 influx over the indicated time n=9-12 myofibers per group from two independent isolations. Scale bar 50µm **(D)** Running distance during eccentric exercise regime of 6 months old male control (n=6) and *Myf5Cre-Pcyt2* (n=4) mice. **(E)** Representative histological analysis (H&E staining) of quadriceps muscles isolated from untrained (no training) 6 months old male control (n=4) or *Myf5Cre-Pcyt2 mice* (n=4) and from 6 months old control (n=6) or *Myf5Cre-Pcyt2 mice* (n=4) after eccentric exercise (training). Black and blue arrows show inflammation and ectopic fat deposits. Scale bars 100µm **(F)** Myopathy scores in 6 months old male control (n=6) and *Myf5Cre-Pcyt2* (n=4) mice following eccentric exercise. The following parameters were used: inflammation, myofiber necrosis, atrophy, interstitial fibrosis, loss of membrane integrity, regenerating myofibers. Each was scored with 1-4 depending of the severity, and summed. **(G)** Blood muscle creatine kinase levels inferred from muscle creatine kinase activity from 6 months old sedentary and immediately after eccentric exercise of male control and Myf5Cre-Pcyt2 mice. **(H)** F-actin staining of skeletal muscle tissue isolated from 6 months old male control and *Myf5Cre-Pcyt2* mice after eccentric exercise. Images of quadriceps cross-sections were taken using 20x magnifications. ≥100 myofibers were counted. n=3 mice per group. Scale bar 15µm**.**

Data are shown as means ± SEM. Each dot represents data point from individual mice unless stated otherwise. *$p < 0.05$, **$p < 0.01$, ***$p < 0.001$, and ****$p < 0.0001$, n.s. not significant. Unpaired Student t-test with Welch correction was used for statistical analysis unless stated otherwise.

Figure 7. Adenovirus based *Pcyt2* gene therapy in mice is efficient for treatment of Pcyt2 deficiency-induced muscle pathology.

(A) Scheme of Pcyt2 muscle specific gene therapy. **(B)** Grip strength of male control (saline) *Myf5Cre-Pcyt2 (saline) and Myf5Cre-Pcyt2 (AAV6-CK8-Pcyt2HA)* mice. **(C)** Muscle weight

isolated from 6 months old male control, *Myf5Cre-Pcyt2 saline* treated *and Myf5Cre-Pcyt2 AAV6-Pcyt2* treated mice. Each dot represents single mice. QA, quadriceps; GC, gastrocnemius; TA, tibialis anterior muscles. Scale bars 1 cm**. (D)** Assessment of Pcyt2HA expression in *Myf5Cre-Pcyt2 AAV6-Pcyt2* treated male mice as determined by quadriceps lysate anti-HA immunoprecipitation, followed by anti-Pcyt2 blot, 6 months after the gene delivery. **(E)** Total phosphatidylethanolamine levels from quadriceps of control, *Myf5Cre-Pcyt2 saline* treated *and Myf5Cre-Pcyt2 AAV6-Pcyt2* treated male mice, 6 months after the treatment. **(F)** Myofiber diameter sizes from 6 months old control (n=5 mice and ≥ 60 myofibers analyzed per mouse), *Myf5Cre-Pcyt2 saline* treated (n=5 mice and ≥ 60 myofibers analyzed per mouse), and *Myf5Cre-Pcyt2 AAV6-Pcyt2* mice (n=5 mice and ≥ 60 myofibers analyzed per mouse). Myofibers were imaged using 10X magnification. Scale bar 100µm**. (G)** Polarization microscopy of NR12S-stained muscle-derived GPMVs from control (n=84), *Myf5Cre-Pcyt*2 saline (n=93) and *Myf5Cre-Pcyt*2 AAV6-*Pcyt2* treated (n=88) 6 months old male mice. GPMVs were derived from three independent isolations. Each dot represents values of a single GPMV. Scale bar 5µm. **(H)** Surface stiffness analysis by Brillouin frequency shift (BFS) from isolated myofibers of control, *Myf5Cre-Pcyt*2 saline and *Myf5Cre-Pcyt*2 AAV6-*Pcyt2* treated 6 months old male mice. Each data point in the right panel represents a BFS peak value of the myofiber surface. 20 myofibers from n=4 male mice per group. **(I)** Muscle mitochondrial respiration of control, *Myf5Cre-Pcyt*2 saline and *Myf5Cre-Pcyt*2 AAV6-*Pcyt2* treated mice as assessed by complex I linked activity on muscle lysates isolated from 6 months old male mice. N=5 mice per group. Paired Student t-test was used for statistical analysis. Dashed line indicates the average value of mitochondrial activities measured from 5 individual control male mice.

Data are shown as means ± SEM. Each dot represents data point from individual mice unless stated otherwise. *p < 0.05, **p < 0.01, ***p < 0.001, and ****p < 0.0001, n.s. not significant. Unless otherwise indicated, Multiple comparison One-Way ANOVA with Dunnett correction was used for statistical analysis unless stated otherwise.

Figure 8. Pcyt2 activity is reduced in aged muscles from humans and mice and *Pcyt2* gene delivery ameliorates age-related atrophy in sarcopenic mice.

(A) PCYT2 activity in quadriceps from young (20-30yr) and middle aged (45-62yr) healthy human volunteers. Each dot represents individual human. **(B)** Pcyt2 activity in quadriceps from young (6 month) and pre-sarcopenic (24 months old) C57B6/J male mice. **(C)** Lipidomics analyses from quadriceps isolated from young (6 months old) and pre-sarcopenic (24 months old) C57B6/J male mice. mice. Data are shown relative to control values. CE-cholesterol ester; Cer-Ceramides; DAG-diacylglycerols; LPC-lysophosphatidylcholines; LPE-lysophosphatidylethanolamines; PC-phosphatidylcholines; PE-phosphatidylethanolamines; PG-phosphatidylglycerols; PI-phosphatidylinositols; PS-phosphatidylserines; SM-sphingomyelins; TAG-triacylglycerols. n=5 mice per group. **(D)** Scheme of adenovirus based, muscle-specific delivery of Pcyt2 to pre-sarcopenic 24 months old C57B6/J male mice. **(E)** Assessment of Pcyt2HA expression as determined by anti-HA immunoprecipitation, followed by an anti-Pcyt2 blot, from quadriceps isolated 2 months after the gene delivery. **(F)** Total phosphatidylethanolamine levels from quadriceps of young (6 months old), and aged (26 months old) control (saline) and *AAV6-CK8-Pcyt2HA* transduced C57B6/J male mice two months after AAV6 injection. **(G)** Polarization microscopy of NR12S-stained GPMVs isolated from aged (26 months old) control (n=63) (saline) and *AAV6-CK8-Pcyt2HA* transduced (n=79) C57B6/J male mice two months after AAV6 injection. GPMVs were derived from three independent isolations. Each dot represents values of a single GPMV. Scale bar 10μm. **(H)** Surface stiffness analysis as measured by Brillouin frequency shift (BFS) from isolated myofibers of aged (26 months old) control (saline) and *AAV6-CK8-Pcyt2HA* transduced C57B6/J male mice two months after AAV6 injection. Dashed line indicates the average value of Brillouin frequency shift (BFS) measured separately from five 6 month old male mice. Each data point in the right panel represents a BFS peak value of the myofiber surface. 7 myofibers from n=7 mice per group were analyzed. **(I)** Muscle mitochondrial function of aged (26 months old) control (saline) and *AAV6-CK8-Pcyt2HA* transduced C57B6/J male mice two months after the treatment as measured by complex I linked activity. Paired Student t-test was used for statistical analysis. Dashed line indicates the average value of mitochondrial activities measured separately from five 6 month old male mice. **(J)** Myofiber diameter sizes from aged (26 months old) control (saline) (n=5 mice and ≥ 180 myofibers analyzed per mouse.) and *AAV6-CK8-Pcyt2HA* transduced C57B6/J male mice (n=5 mice and ≥ 180 myofibers analyzed per mouse) two months after the AAV6 injection. Dashed line indicates the average value of myofiber diameter sizes measured separately from five 6 months old

male mice (≥ 60 myofibers analyzed per mouse). Scale bar 100µm**. (K)** Grip strength measurements on aged (26 months old) control (saline; n=15) and *AAV6-CK8-Pcyt2HA* transduced (n=11) C57B6/J male mice one and two months after AAV6 injection. Repeated Measures Two-Way ANOVA with Bonferroni correction was used for statistical analysis.

Data are shown as means ± SEM. Each dot represents data point from individual mice unless stated otherwise. *p < 0.05, **p < 0.01, ***p < 0.001, and ****p < 0.0001, n.s. not significant. Unpaired Student t-test with Welch correction was used for statistical analysis unless stated otherwise.

Methods

Studies in Humans

Patients

Patients with *PCYT2* and *EPT1* deficiency were identified previously[6,8]. Their height and weight were recorded at visits to the hospital. The spinal MRI was performed at the age of 19 years. All data presented are being shared with parental and patient consent under the ethical approval according to institutional and international guidelines for studies with human subjects.

Human biopsies

All human experiments were approved by the regional ethical review board in Stockholm (2014/516-31/2 and 2010/786-31/3) and complied with the Declaration of Helsinki. Oral and written informed consent were obtained from all subjects prior to participation in the study. 8 healthy young adults (age 21-29) and 8 middle-aged (age 45-62) subjects were recruited. The subjects did not use any medications and were nonsmokers. Biopsies of the quadriceps vastus lateralis muscle were obtained under local anesthesia using the Bergström percutaneous needle biopsy technique and immediately frozen in isopentane, cooled in liquid nitrogen, and stored at −80°C until further analysis.

Studies in zebrafish

Generation of mutant zebrafish and analysis

Zebrafish were raised and maintained at the biological services facility at the University of Manchester under standard conditions. Pcyt2 mutant zebrafish at F0 have been described previously [6]**.** For histological examination, animals were sacrificed by lethal anesthesia with buffered tricaine methanesulfonate. After gross examinations, whole body was fixed in 4% paraformaldehyde (PFA) for 72 hr. After fixation, 0.5 mm pieces were cut and embedded in paraffin blocks. 3µm sections were further processed for routine hematoxylin and eosin

staining. Back muscle cross sectional areas of the same anatomical region were imaged under 10X magnification, followed by analysis with ImageJ software. All animal experiments were approved by the Animal Care and Use Committee at the University of Manchester.

Studies in mice

Mouse lines and diets

All mice were housed in the IMBA mouse colony with a 12 h light/dark cycle in a temperature-controlled environment and fed a standard chow diet. *Pcyt2* conditional mice have been described previously[73]. In all cases, all mice described in our experiments were littermates, matched for age and sex. Tissue specific *Pcyt2* mutant mice were generated by crossing of *Pcyt2*$^{flox/flox}$ mice with Cre transgenic mice. *Villin* Cre mice originate from Institut Curie (Sylvie Robine Lab). The following mouse lines were obtained from the Jackson Laboratory (Jackson Lab, Bar Harbor, US): *Adipoq* Cre (B6;FVB-Tg(Adipoq-cre)1Evdr/J); *Alb* Cre (B6.Cg-Speer6-ps1Tg(Alb-cre)21Mgn/J); *Mck* Cre (B6.FVB(129S4)-Tg(Ckmm-cre)5Khn/J. All animal experiments were approved by the Animal Care and Use Committee at IMBA, University of Physical Education in Budapest, Institut NeuroMyoGène and Institut de Recherche en Santé Digestive in Toulouse.

Functional *in vivo* muscle tests

Grip strength: Two-, 4- and 6-month-old mice (control and Pcyt2 Myf5 KO mice) were subjected to grip strength tests using a grip strength meter (Bioseb, USA). Prior to tests, mice were single caged for two weeks. Clasping index was evaluated as described previously[74]**.** Each mouse was scored three times, and an average of scores was calculated.

Eccentric exercise: Single caged mice were acclimatized for treadmill exercise for three days on low speed (4m min^{-1} for 40 min per day), followed by a 7-day training on a medium speed (4m min^{-1} for 40 min plus 9m min^{-1} for 20 min per day), and a 2-day stress training (20m min-1 for 20min per day). Immediately after the completion of the exercise, mice were sacrificed, and muscles were collected for histological analysis.

Synergic muscle ablation: For synergic ablation experiments, all surgical procedures were performed under aseptic conditions with the animals deeply anaesthetized with

pentobarbital sodium (60 mg/kg i.p.). Compensatory overload of the plantaris muscle was performed unilaterally via removal of the major synergistic muscles (gastrocnemius-medialis, -lateralis and soleus). A sham operation was systematically performed on the control hindlimb, which consisted of separating tendons of the soleus and gastrocnemius muscles from the plantaris muscle. Analgesic was administered to the animals for two days following the operation. The overload lasted for 14 days. For maintaining the activity of the animals during the overload period, moderate speed walking training was used on a treadmill (10 degrees ascents, 4-5 m/min, 30 min, 6 times/week). At the end of this period, after animal sacrifice, the plantaris muscle was removed bilaterally, trimmed of excess fat and connective tissue, weighed and processed for further analysis.

AAV-based vector delivery: For the AAV6 treatment, Pcyt2 (NM_024229.3) was C-terminally tagged with an HA-tag and cloned into the AAV6-CK8 muscle specific expression vector [47] using the Sal1-Kpn1 restriction sites. AAV6 viral particles were prepared as previously described [75]. For gene therapy of Myf5Cre-Pcyt2 mutant mice, 4 days old pups were injected i.p. with $2x10^{11}$ vector genomes per mouse. For ageing studies 24-month-old C57B6/J mice (Jackson Labs, Bar Harbor) were single caged for two weeks for acclimatization. Grip strength was measured before AAV6 delivery using the grip strength meter. On the day of the AAV injection, mice were anesthetized with isoflurane, and injected retro-orbitally either with AAV6-Pcyt2HA ($5x10^{12}$ vector genomes per mouse) or as a control saline. Expression of the Pcyt2-HA was determined by Western blotting and grip strength was measured one and two months after the injection.

Metabolic studies: Animals were fed standard chow diet and blood glucose was measured at fed and fasted state (16h fasting). Standard chow diet was purchased from SSNIFF (V 1184-300; 10mm pellets autoclavable; 49% kcal carbohydrates, 36% kcal protein and 15% kcal fat). Measurements were done at the same time of the day by using Onetouch Verio strips (LifeScan, GmbH) after tail snipping. Food consumption was measured on single cage housed animals over a period of two weeks, after one week acclimatization. For calorimetry, measurements were performed at room temperature (21C-23C) on a 12/12 h light/dark cycle in a PhenoMaster System (TSEsystems, Bad Homburg, Germany) using an open circuit calorimetry system. Mice (4-7 months old) were housed individually, trained on drinking nozzles for 7 days and allowed to adapt to the PhenoMaster chamber for 2 days. Food and

water were provided ad libitum. Parameters of indirect calorimetry and activity were determined for 5 consecutive days. Body weights were recorded at the beginning and end of the experiments and average values were plotted against energy expenditure and activity. To address brown fat activity, 6-month-old mice were housed at 4°C and body temperature was measured during the fed period using a thermometer (Thermometer TK 98802; Bioseb). Temperature was recorded every hour over a 4 h period. After a 2 days recovery period at room temperature, the same mice were fasted and the body temperatures determined at 6 and 16 hours of fasting. For autophagy induction, animals were fasted for 24 hours.

Isolation and imaging of Giant Plasma Membrane Vesicles (GPMVs)

GPMVs were prepared as previously described [76]. Briefly, myoblasts were seeded on a 60 mm petri dish until ~ 70% confluency. Before GPMV formation, they were washed twice with GPMV buffer (150 mM NaCl, 10 mM Hepes, 2 mM $CaCl_2$, pH 7.4) and finally 2 ml of GPMV buffer with 25 mM PFA and 10 mM DTT (final concentrations) was added. After incubation for 2hr at 37^{o}C, GPMVs were collected from the supernatant. For GMPV preparation from myofibers, the extensor digitorum longus (EDL) muscle was digested in collagenase supplemented medium (type1, 2mg/mL) for 2.5hr at 37^{o}C, followed by single myofiber isolation. Myofibers were then gently washed twice with FCS free DMEM, followed by a brief 1min wash with GPMV buffer containing 25 mM PFA, to prevent myofiber hypercontraction. Finally, GPMV buffer with 25 mM PFA and 10 mM DTT was added to the myofibers. After incubation for 2hr at 37^{o}C, GPMVs were collected from the supernatant. GMPVs were labelled with the polarity sensitive membrane probe NR12S (a kind gift from A. Klymchenko) at 0.1µg/ml final probe concentration in phosphate buffered saline (PBS) for 5 minutes and then imaged on a Zeiss LSM 780 confocal microscope equipped with a 32-channel GaAsP detector array. Laser light at 488 nm was used for fluorescence excitation of NR12S. The lambda detection range was set between 490 - 691 nm. Images were analyzed by using a custom plug-in compatible with Fiji/ImageJ3 to measure generalized polarization which reflects membrane lipid packing/order using the following formula where I_{560} and I_{650} are the fluorescence intensities at 560 nm and 650 nm respectively:

$$GP = \frac{I_{560} - I_{650}}{I_{560} + I_{650}}$$

Brillouin Microscopy of myofibers

Brillouin Light Scattering Microscopy (BLSM) was performed using an inverted confocal sample-scanning microscope with a Brillouin imaging-spectrometer as described previously [42,77]. Briefly the setup employed a 532nm single-frequency probing laser and is based on a 2-stage cross dispersion Virtual Imaged Phase Array (VIPA) with intermediate Fourier and image plane filtering, a cooled EM-CCD camera (Hamamatsu ImagEMII) for detection, with a spectral finesse >85. For more scattering samples, we also employed a heated Iodine absorption cell in the detection path tuned to the laser wavelength to reduce the elastic scattering signal. To generate spatial maps, samples were scanned with a 3-axis piezo electric stage (Physik Instrumente). Imaging was performed through 1.3 Numerical Aperture (NA) Si immersion-oil objective (Olympus) and confocality was assured via a physical pinhole of ~1 Airy Unit (AU) before coupling the light into the spectrometer. Widefield transmitted light images were used to determine the scanning area for each sample. Several cross-sectional scans were performed for each myofiber at positions separated by a 1µm. Acquisition was controlled by a custom Labview based script developed by the company THATec. The acquisition (dwell) time per voxel was 100ms and the power measured at the sample was 2-3mW. Each measured spectrum was de-convolved with the complete system spectral response as determined for the attenuated elastic scattering peak measured prior to each scan in the same sample. Prior and subsequent to each imaging session the spectra of water and ethanol were measured on a separate imaging arm and used for calibrating the spectral projection based on paraxial theory [78], adapted to a dual VIPA setup. Each spectrum was then analyzed in Matlab (Mathworks) using custom developed scripts employing Spectral Phasor Analysis. Results were confirmed to be in agreement with ones obtained from conventional non-linear least-squares fitting of deconvolved spectra consisting of the Stokes and Anti-Stokes Brillouin peaks using Lorentzian functions. The extracted Brillouin peak frequency, which scales with the local elastic storage modulus, is taken for local stiffness. All measurements were performed at 37^{o}C and 5% CO2.

Atomic force microscopy

Force spectroscopy by means of Atomic force microscopy was done on individual myofibers after isolation from EDL muscles. Fibers were either cultured on matrigel coated dishes (QI mode) or probed immediately after isolation (Force spectroscopy). A JPK (Bruker) Nanowizard4 AFM atomic force microscope was used for the AFM experiments. The QP-BioAC cantilevers from Nanosensors (0.06N/m, less than 10 nm nominal tip radius) were used because of their ability to work in QI mode with biological samples. The approach and retract speeds were kept constant at 52microns/s. The model used to obtain the Young's modulus from the acquired data was Hertz/Sneddon. The paraboloid model was chosen as the most suitable for the sharp tips of the QP-BioAC cantilevers. For the fits forces up to 60pN were considered, where indentation depths remained below 500nm. Each of the fibers retrieved ≥ 4000 values (5µm X 5µm sampled in 64x64 data pixels). Matlab's Randsample function was used to uniformly sample 500 data points. For the force curves acquired for the qualitative comparison, forces up to 600pN were applied to a single location each, using same cantilevers and approach speeds. Samples were kept at a 37^{o}C during the experiment.

Laser-induced damage of myofiber cell membranes

Myofibers were freshly isolated from EDL muscle of 4-month old mice by digestion in collagenase supplemented media (type1, 2mg/ml, Sigma) for 2 hr at 37^{o}C. After digestion, individual fibers were transferred onto a 4-well chamber slide (Nunc Lab-Tek, Merck, GmbH) containing HBSS with 2.5µM FM1-43 dye (Molecular Probes, Invitrogen, ThermoFisher Scientific, GmbH). Laser-induced cell membrane damage was performed as previously described [45]. Briefly, a 5 × 5 pixel area of the plasma membrane was exposed to a Laser at 20% of maximum power (Enterprise, 80 mW, 351/364 nm) for 5 s using a Zeiss-LSM 510 confocal microscope equipped with a ×63 water immersion lens (N.A. 1.3). Following the laser damage, distribution of the FM1-43 dye was imaged using high speed video captures. Throughout the experiment, cells were kept at a 37^{o}C in a 5% CO_2 chamber.

Ca^{2+} dynamics under voltage-clamp protocol

The flexor digitorum brevis (FDB) and interosseous (IO) muscles were freshly isolated from mice and incubated with collagenase (Sigma type 1) for 1 hour at 37 °C in a Tyrode solution. Single myofibers were isolated by gentle mechanical trituration of the collagenase-treated muscles within the experimental chamber. Fibers were voltage-clamped using the silicone-voltage-clamp technique as described[79] with the voltage-clamp pipette filled with a solution containing (in mM) 140 K-glutamate, 5 Na2-ATP, 5 Na2-phosphocreatine, 5.5 MgCl2, 5 glucose, 5 HEPES and either 15 EGTA, 6 CaCl2, and 0.1 rhod-2 or 0.1 fluo-4FF. The extracellular solution contained (in mM) 140 TEA-methane-sulfonate, 2.5 CaCl2, 2 MgCl2, 1 4-aminopyridine, 10 HEPES and 0.002 tetrodotoxin. For fluo-4FF fluorescence measurements, the extracellular solution also contained 0.05 mM N-benzyl-p-toluene sulfonamide (BTS) to block contraction. All solutions were at pH 7.2. Voltage-clamp and membrane current measurements were done with an RK-400 patch-clamp amplifier (Bio-Logic, Claix, France) in whole-cell voltage-clamp configuration. Command voltage pulse generation was achieved with an analog-digital converter (Digidata 1440A, Axon Instruments, Foster City, CA) controlled by pClamp 9 software (Axon Instruments). Holding voltage was always set to -80 mV. Following insertion of the micropipette extremity into the muscle fiber, a 30 min-long period of equilibration was allowed before taking measurements. Rhod-2 and fluo-4-FF fluorescence were detected with a Zeiss LSM 5 Exciter confocal microscope equipped with a 63× oil immersion objective (numerical aperture 1.4). For detection of rhod-2 and fluo-4 FF fluorescence, excitation was from the 543 nm line of a HeNe laser and from the 488 nm line of an Argon laser, respectively, and fluorescence was collected above 560 nm and above 505 nm, respectively. Both rhod-2 and fluo-4 FF voltage-activated fluorescence changes were imaged using the line-scan mode (x,t) of the system and expressed as F/F0 where F0 is the baseline fluorescence. Rhod-2 Ca2+ transients were triggered by 0.5 s-long depolarizing pulses of increasing amplitude. From these, the rate of SR calcium release (d[CaTot]/dt) was calculated as described[80] Fluo-4-FF was used under non-EGTA buffering intracellular conditions to assess the resistance of the fibers to a fatigue protocol. Fibers were stimulated by consecutive trains of thirty 5 ms-long pulses from -80 mV to +60 mV delivered at 100 Hz: 40 trains were applied, separated by a 0.7 s interval.

***In vivo* muscle permeability measurements**

To determine in vivo muscle tissue permeability, 1% Evans blue dye (10 ml kg^{-1} body weight, Sigma, GmbH) was injected into the intraperitoneal cavity of 8 month old animals. 16hours later mice were sacrificed via cervical dislocation and muscles collected. Quadriceps muscles were weighed and then soaked in formamide (GibcoBRL, UK) for 48 hr at 55^{o}C with gentle shaking. The optical density of Evans blue in the resulting supernatant was measured at 610 nm with a Spectronic 610 spectrophotometer (Milton Roy). To image Evans blue via microscopy, muscles were immediately embedded in OCT and frozen. 10µm longitudinal sections were cut and visualized after counterstaining with DAPI.

Pcyt2 enzyme activity

Frozen muscle tissue (50mg) was homogenized in a cold lysis buffer (10 mM Tris-HCl [pH 7.4], 1 mM EDTA, and 10 mM NaF) and briefly centrifuged to remove cell debris. Fifty ug of protein was assayed with 0.2 µCi of [14C]-phosphoethanolamine (P-Etn) (American Radiolabeled Chemical) in 50µl of reaction mixture of 50 mM MgCl2, 50 mM DTT, 10 mM unlabeled P-Etn, 20 mM CTP and 100 mM Tris-HCl (pH 7.8). The reaction was incubated at 37^{0}C for 15 min and terminated by boiling (2 min). The reaction product [14C]CDP-Etn was separated from [14-C]PEtn on Silica gel G plates (Analtech) with a solvent system of methanol:0.5%NaCl:ammonia (10:10:1). CDP- Etn and P-Etn in standards and samples were visualized with a 0.5% ninhydrin in ethanol and the [14C]CDP-Etn collected and quantified by liquid-scintillation counting. Pcyt2 activity was expressed in nmol/min/mg protein. Protein content was determined with bicinchronic acid assay from Pierce.

Further methods can be found in Supplementary Information.

Statistical analysis of mouse studies

All mouse data are expressed as mean +/- standard error of the mean (SEM). All figures and mouse statistical analyses were generated using Prism 8 (GraphPad) or R. Details of the statistical tests used are stated in the figure legends. In all figures, statistical significance is represented as *P <0.05, **P <0.01, ***P <0.001, ****P <0.0001.

Data availability

The authors declare that [the/all other] data supporting the findings of this study are available within the paper [and its supplementary information files]. The data that support the findings of this study are available from the corresponding authors upon request. The original datasets used in the RNA sequencing analysis can be accessed at NCBI archived under GEO accession codes GSM6785661, GSM6785662, GSM6785663, GSM6785664, GSM6785665 and GSM6785666. Mass spectrometry lipidomics source data for Figures. 1,4, 8 and Extended Data Figures 7 are provided under Supplementary information with the paper. Further information and requests for resources and reagents should be directed to and will be fulfilled by the Lead Contacts Josef M. Penninger (josef.penninger@ubc.ca) or Domagoj Cikes (domagoj.cikes@imba.oeaw.ac.at).

References

1. Davies, K. E. & Nowak, K. J. Molecular mechanisms of muscular dystrophies: Old and new players. *Nature Reviews Molecular Cell Biology* (2006) doi:10.1038/nrm2024.

2. Wilkinson, D. J., Piasecki, M. & Atherton, P. J. The age-related loss of skeletal muscle mass and function: Measurement and physiology of muscle fibre atrophy and muscle fibre loss in humans. *Ageing Research Reviews* (2018) doi:10.1016/j.arr.2018.07.005.

3. Shevchenko, A. & Simons, K. Lipidomics: Coming to grips with lipid diversity. *Nature Reviews Molecular Cell Biology* (2010) doi:10.1038/nrm2934.

4. Harayama, T. & Riezman, H. Understanding the diversity of membrane lipid composition. *Nature Reviews Molecular Cell Biology* (2018) doi:10.1038/nrm.2017.138.

5. Gibellini, F. & Smith, T. K. The Kennedy pathway-de novo synthesis of phosphatidylethanolamine and phosphatidylcholine. *IUBMB Life* (2010) doi:10.1002/iub.337.

6. Vaz, F. M. *et al.* Mutations in PCYT2 disrupt etherlipid biosynthesis and cause a complex hereditary spastic paraplegia. *Brain* (2019) doi:10.1093/brain/awz291.

7. Ahmed, M. Y. *et al.* A mutation of EPT1 (SELENOI) underlies a new disorder of Kennedy pathway phospholipid biosynthesis. *Brain* (2017) doi:10.1093/brain/aww318.

8. Horibata, Y. *et al.* EPT1 (selenoprotein I) is critical for the neural development and maintenance of plasmalogen in humans. *J. Lipid Res.* (2018) doi:10.1194/jlr.P081620.

9. Horibata, Y. & Hirabayashi, Y. Identification and characterization of human ethanolaminephosphotransferase. *J. Lipid Res.* (2007) doi:10.1194/jlr.C600019-JLR200.

10. Uhlén, M. *et al.* Tissue-based map of the human proteome. *Science (80-.).* (2015)

doi:10.1126/science.1260419.

11. Naef, V. *et al.* Swimming in Deep Water: Zebrafish Modeling of Complicated Forms of Hereditary Spastic Paraplegia and Spastic Ataxia. *Frontiers in Neuroscience* (2019) doi:10.3389/fnins.2019.01311.

12. Fassier, C., Hazan, J. & Melki, J. Mouse Models of Autosomal Dominant Spastic Paraplegia. in *Movement Disorders: Genetics and Models: Second Edition* (2015). doi:10.1016/B978-0-12-405195-9.00070-6.

13. Blackstone, C. Murine Models of Autosomal Recessive Hereditary Spastic Paraplegia. in *Movement Disorders: Genetics and Models: Second Edition* (2015). doi:10.1016/B978-0-12-405195-9.00071-8.

14. Rapisarda, R., Muntoni, F., Gobbi, P. & Dubowitz, V. Duchenne muscular dystrophy presenting with failure to thrive. *Arch. Dis. Child.* (1995) doi:10.1136/adc.72.5.437.

15. Fullerton, M. D., Hakimuddin, F. & Bakovic, M. Developmental and Metabolic Effects of Disruption of the Mouse CTP:Phosphoethanolamine Cytidylyltransferase Gene (Pcyt2). *Mol. Cell. Biol.* (2007) doi:10.1128/mcb.01527-06.

16. Francetic, T. & Li, Q. Skeletal myogenesis and Myf5 activation. *Transcription* (2011) doi:10.4161/trns.2.3.15829.

17. White, R. B., Biérinx, A. S., Gnocchi, V. F. & Zammit, P. S. Dynamics of muscle fibre growth during postnatal mouse development. *BMC Dev. Biol.* (2010) doi:10.1186/1471-213X-10-21.

18. Demonbreun, A. R., Biersmith, B. H. & McNally, E. M. Membrane fusion in muscle development and repair. *Seminars in Cell and Developmental Biology* vol. 45 (2015).

19. Emoto, K. & Umeda, M. An Essential Role for a Membrane Lipid in Cytokinesis. *J. Cell Biol.* **149**, (2000).

20. Mccarthy, J. J. *et al.* Effective fiber hypertrophy in satellite cell-depleted skeletal muscle. *Development* (2011) doi:10.1242/dev.068858.

21. Archer, J. E., Gardner, A. C., Roper, H. P., Chikermane, A. A. & Tatman, A. J. Duchenne

muscular dystrophy: the management of scoliosis. *J. Spine Surg.* (2016) doi:10.21037/jss.2016.08.05.

22. Seale, P. *et al.* PRDM16 controls a brown fat/skeletal muscle switch. *Nature* (2008) doi:10.1038/nature07182.

23. Eguchi, J. *et al.* Transcriptional control of adipose lipid handling by IRF4. *Cell Metab.* (2011) doi:10.1016/j.cmet.2011.02.005.

24. Weiland, D. *et al.* Imbalance of Mitochondrial Respiratory Chain Complexes in the Epidermis Induces Severe Skin Inflammation. *J. Invest. Dermatol.* (2018) doi:10.1016/j.jid.2017.08.019.

25. Shin, J. M. *et al.* Targeted deletion of Crif1 in mouse epidermis impairs skin homeostasis and hair morphogenesis. *Sci. Rep.* (2017) doi:10.1038/srep44828.

26. Nguyen, T. T. *et al.* Loss of Miro1-directed mitochondrial movement results in a novel murine model for neuron disease. *Proc. Natl. Acad. Sci. U. S. A.* (2014) doi:10.1073/pnas.1402449111.

27. Choi, M. J. *et al.* An adipocyte-specific defect in oxidative phosphorylation increases systemic energy expenditure and protects against diet-induced obesity in mouse models. *Diabetologia* (2020) doi:10.1007/s00125-019-05082-7.

28. Vernochet, C. *et al.* Adipose tissue mitochondrial dysfunction triggers a lipodystrophic syndrome with insulin resistance, hepatosteatosis, and cardiovascular complications. *FASEB J.* (2014) doi:10.1096/fj.14-253971.

29. Sustarsic, E. G. *et al.* Cardiolipin Synthesis in Brown and Beige Fat Mitochondria Is Essential for Systemic Energy Homeostasis. *Cell Metab.* (2018) doi:10.1016/j.cmet.2018.05.003.

30. Srivillibhuthur, M. *et al.* TFAM is required for maturation of the fetal and adult intestinal epithelium. *Dev. Biol.* (2018) doi:10.1016/j.ydbio.2018.04.015.

31. Selathurai, A. *et al.* The CDP-Ethanolamine Pathway Regulates Skeletal Muscle Diacylglycerol Content and Mitochondrial Biogenesis without Altering Insulin

Sensitivity. *Cell Metab.* (2015) doi:10.1016/j.cmet.2015.04.001.

32. Beedle, A. M. *et al.* Mouse fukutin deletion impairs dystroglycan processing and recapitulates muscular dystrophy. *J. Clin. Invest.* (2012) doi:10.1172/JCI63004.

33. Potthoff, M. J. *et al.* Regulation of Skeletal Muscle Sarcomere Integrity and Postnatal Muscle Function by Mef2c. *Mol. Cell. Biol.* (2007) doi:10.1128/mcb.01187-07.

34. Brüning, J. C. *et al.* A muscle-specific insulin receptor knockout exhibits features of the metabolic syndrome of NIDDM without altering glucose tolerance. *Mol. Cell* (1998) doi:10.1016/S1097-2765(00)80155-0.

35. Chamberlain, J. S., Jaynes, J. B. & Hauschka, S. D. Regulation of creatine kinase induction in differentiating mouse myoblasts. *Mol. Cell. Biol.* (1985) doi:10.1128/mcb.5.3.484.

36. Schlame, M., Xu, Y., Erdjument-Bromage, H., Neubert, T. A. & Ren, M. Lipidome-wide 13C flux analysis: A novel tool to estimate the turnover of lipids in organisms and cultures. *J. Lipid Res.* (2020) doi:10.1194/jlr.D119000318.

37. Van Meer, G., Voelker, D. R. & Feigenson, G. W. Membrane lipids: Where they are and how they behave. *Nature Reviews Molecular Cell Biology* (2008) doi:10.1038/nrm2330.

38. Nair, U. *et al.* A role for Atg8-PE deconjugation in autophagosome biogenesis. *Autophagy* (2012) doi:10.4161/auto.19385.

39. Martinez-Lopez, N. *et al.* Autophagy in Myf5+ progenitors regulates energy and glucose homeostasis through control of brown fat and skeletal muscle development. *EMBO Rep.* (2013) doi:10.1038/embor.2013.111.

40. Roses, A. D. & Appel, S. H. Inherited Membrane Disorders of Muscle: Duchenne Muscular Dystrophy and Myotonic Muscular Dystrophy. in *Physiology of Membrane Disorders* (1978). doi:10.1007/978-1-4613-3958-8_38.

41. Steinkühler, J., Sezgin, E., Urbančič, I., Eggeling, C. & Dimova, R. Mechanical properties of plasma membrane vesicles correlate with lipid order, viscosity and cell

density. *Commun. Biol.* (2019) doi:10.1038/s42003-019-0583-3.

42. Elsayad, K. *et al.* Mapping the subcellular mechanical properties of live cells in tissues with fluorescence emission-Brillouin imaging. *Sci. Signal.* (2016) doi:10.1126/scisignal.aaf6326.

43. Demonbreun, A. R. & McNally, E. M. Plasma Membrane Repair in Health and Disease. *Curr. Top. Membr.* (2016) doi:10.1016/bs.ctm.2015.10.006.

44. Hamer, P. W., McGeachie, J. M., Davies, M. J. & Grounds, M. D. Evans Blue Dye as an in vivo marker of myofibre damage: Optimising parameters for detecting initial myofibre membrane permeability. *J. Anat.* (2002) doi:10.1046/j.0021-8782.2001.00008.x.

45. Bansal, D. *et al.* Defective membrane repair in dysferlin-deficient muscular dystrophy. *Nature* (2003) doi:10.1038/nature01573.

46. Hody, S., Croisier, J. L., Bury, T., Rogister, B. & Leprince, P. Eccentric muscle contractions: Risks and benefits. *Frontiers in Physiology* (2019) doi:10.3389/fphys.2019.00536.

47. Ramos, J. N. *et al.* Development of Novel Micro-dystrophins with Enhanced Functionality. *Mol. Ther.* (2019) doi:10.1016/j.ymthe.2019.01.002.

48. Crudele, J. M. & Chamberlain, J. S. AAV-based gene therapies for the muscular dystrophies. *Human Molecular Genetics* (2019) doi:10.1093/hmg/ddz128.

49. Gault, M. L. & Willems, M. E. T. Aging, functional capacity and eccentric exercise training. *Aging and Disease* (2013) doi:10.14336/AD.2013.0400351.

50. Manfredi, T. G. *et al.* Plasma creatine kinase activity and exercise-induced muscle damage in older men. *Med. Sci. Sports Exerc.* (1991) doi:10.1249/00005768-199109000-00006.

51. Roth, S. M. *et al.* High-volume, heavy-resistance strength training and muscle damage in young and older women. *J. Appl. Physiol.* (2000) doi:10.1152/jappl.2000.88.3.1112.

52. McGreevy, J. W., Hakim, C. H., McIntosh, M. A. & Duan, D. Animal models of

Duchenne muscular dystrophy: From basic mechanisms to gene therapy. *DMM Disease Models and Mechanisms* (2015) doi:10.1242/dmm.018424.

53. Vance, J. E. & Tasseva, G. Formation and function of phosphatidylserine and phosphatidylethanolamine in mammalian cells. *Biochimica et Biophysica Acta - Molecular and Cell Biology of Lipids* vol. 1831 (2013).

54. Kuter, K. *et al.* Adaptation within mitochondrial oxidative phosphorylation supercomplexes and membrane viscosity during degeneration of dopaminergic neurons in an animal model of early Parkinson's disease. *Biochim. Biophys. Acta - Mol. Basis Dis.* **1862**, (2016).

55. Möller, M. N., Lancaster, J. R. & Denicola, A. Chapter 2 The Interaction of Reactive Oxygen and Nitrogen Species with Membranes. *Current Topics in Membranes* (2008) doi:10.1016/S1063-5823(08)00202-0.

56. Yusupov, M. *et al.* Effect of head group and lipid tail oxidation in the cell membrane revealed through integrated simulations and experiments. *Sci. Rep.* (2017) doi:10.1038/s41598-017-06412-8.

57. Ylikallio, E. & Suomalainen, A. Mechanisms of mitochondrial diseases. *Ann. Med.* **44**, (2012).

58. Kaiyrzhanov, R. *et al.* Defective phosphatidylethanolamine biosynthesis leads to a broad ataxia-spasticity spectrum. *Brain* vol. 144 (2021).

59. Felsenthal, N. & Zelzer, E. Mechanical regulation of musculoskeletal system development. *Development (Cambridge)* (2017) doi:10.1242/dev.151266.

60. Zick, M., Stroupe, C., Orr, A., Douville, D. & Wickner, W. T. Membranes linked by trans-SNARE complexes require lipids prone to non-bilayer structure for progression to fusion. *Elife* **2014**, (2014).

61. Budai, Z. *et al.* Impaired skeletal muscle development and regeneration in transglutaminase 2 knockout mice. *Cells* **10**, (2021).

62. Quach, N. L., Biressi, S., Reichardt, L. F., Keller, C. & Rando, T. A. Focal adhesion kinase

signaling regulates the expression of caveolin 3 and β1 integrin, genes essential for normal myoblast fusion. *Mol. Biol. Cell* **20**, (2009).

63. Horsley, V. *et al.* Regulation of the growth of multinucleated muscle cells by an NFATC2-dependent pathway. *J. Cell Biol.* **153**, (2001).

64. Tran, T. H., Shi, X., Zaia, J. & Ai, X. Heparan sulfate 6-O-endosulfatases (Sulfs) coordinate the Wnt signaling pathways to regulate myoblast fusion during skeletal muscle regeneration. *J. Biol. Chem.* **287**, (2012).

65. Meyers, R. M. *et al.* Computational correction of copy number effect improves specificity of CRISPR-Cas9 essentiality screens in cancer cells. *Nat. Genet.* (2017) doi:10.1038/ng.3984.

66. Dawaliby, R. *et al.* Phosphatidylethanolamine is a key regulator of membrane fluidity in eukaryotic cells. *J. Biol. Chem.* (2016) doi:10.1074/jbc.M115.706523.

67. Mitsuhashi, S. *et al.* A congenital muscular dystrophy with mitochondrial structural abnormalities caused by defective de novo phosphatidylcholine biosynthesis. *Am. J. Hum. Genet.* **88**, (2011).

68. Sher, R. B. *et al.* A rostrocaudal muscular dystrophy caused by a defect in choline kinase beta, the first enzyme in phosphatidylcholine biosynthesis. *J. Biol. Chem.* **281**, (2006).

69. De Winter, J. *et al.* PCYT2 mutations disrupting etherlipid biosynthesis: Phenotypes converging on the CDP-ethanolamine pathway. *Brain* vol. 144 (2021).

70. Shavlakadze, T. *et al.* Age-Related Gene Expression Signature in Rats Demonstrate Early, Late, and Linear Transcriptional Changes from Multiple Tissues. *Cell Rep.* (2019) doi:10.1016/j.celrep.2019.08.043.

71. Cree, M. G. *et al.* Intramuscular and liver triglycerides are increased in the elderly. *J. Clin. Endocrinol. Metab.* (2004) doi:10.1210/jc.2003-031986.

72. Pavlovic, Z. & Bakovic, M. Regulation of phosphatidylethanolamine homeostasis-the critical role of CTP: Phosphoethanolamine cytidylyltransferase (Pcyt2). *International*

Journal of Molecular Sciences (2013) doi:10.3390/ijms14022529.

73. Leonardi, R., Frank, M. W., Jackson, P. D., Rock, C. O. & Jackowski, S. Elimination of the CDP-ethanolamine pathway disrupts hepatic lipid homeostasis. *J. Biol. Chem.* (2009) doi:10.1074/jbc.M109.031336.

74. Guyenet, S. J. *et al.* A simple composite phenotype scoring system for evaluating mouse models of cerebellar ataxia. *J. Vis. Exp.* (2010) doi:10.3791/1787.

75. Halbert, C. L., Allen, J. M. & Chamberlain, J. S. AAV6 vector production and purification for muscle gene therapy. in *Methods in Molecular Biology* (2018). doi:10.1007/978-1-4939-7374-3_18.

76. Sezgin, E. *et al.* Elucidating membrane structure and protein behavior using giant plasma membrane vesicles. *Nat. Protoc.* (2012) doi:10.1038/nprot.2012.059.

77. Elsayad, K. *et al.* Mechanical Properties of cellulose fibers measured by Brillouin spectroscopy. *Cellulose* (2020) doi:10.1007/s10570-020-03075-z.

78. Xiao, S., Weiner, A. M. & Lin, C. A dispersion law for virtually imaged phased-array spectral dispersers based on paraxial wave theory. *IEEE J. Quantum Electron.* (2004) doi:10.1109/JQE.2004.825210.

79. Lefebvre, R., Pouvreau, S., Collet, C., Allard, B. & Jacquemond, V. Whole-cell voltage clamp on skeletal muscle fibers with the silicone-clamp technique. *Methods Mol. Biol.* (2014) doi:10.1007/978-1-4939-1096-0_9.

80. Kutchukian, C. *et al.* Phosphatidylinositol 3-Kinase Inhibition restores Ca2+ release defects and prolongs survival in myotubularin-deficient mice. *Proc. Natl. Acad. Sci. U. S. A.* (2016) doi:10.1073/pnas.1604099113.

Figure 1

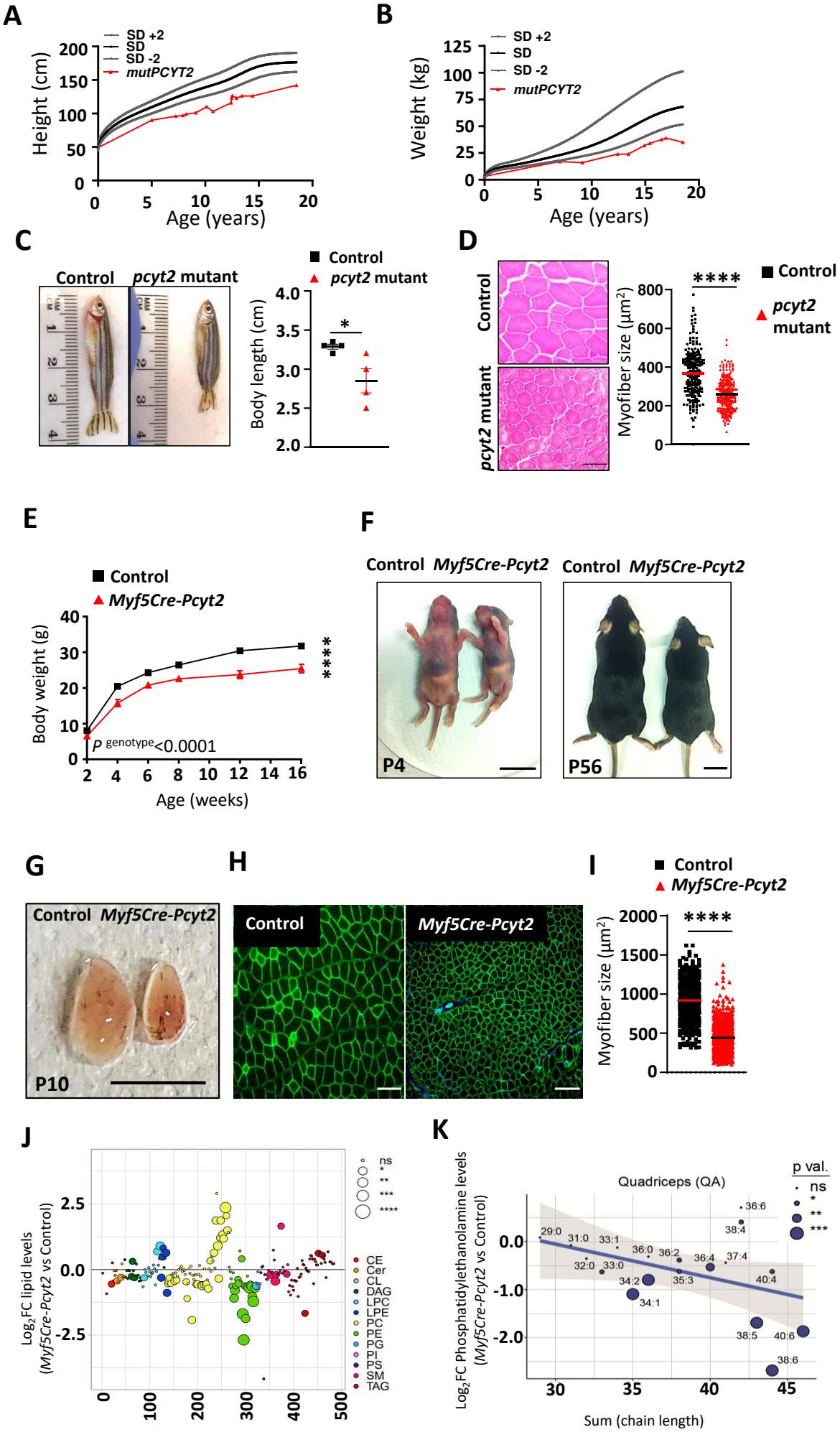
A
SD +2
SD
SD -2
mutPCYT2
Height (cm)
Age (years)
B
Weight (kg)
C
Control
pcyt2 mutant
Body length (cm)
D
Myofiber size (µm²)
****
E
Body weight (g)
P genotype<0.0001
Age (weeks)
Control Myf5Cre-Pcyt2
F
P4
P56
G
P10
H
I
J
Log2FC lipid levels (Myf5Cre-Pcyt2 vs Control)
CE
Cer
CL
DAG
LPC
LPE
PC
PE
PG
PI
PS
SM
TAG
K
Quadriceps (QA)
p val.
Log2FC Phosphatidylethanolamine levels (Myf5Cre-Pcyt2 vs Control)
Sum (chain length)

Figure 2

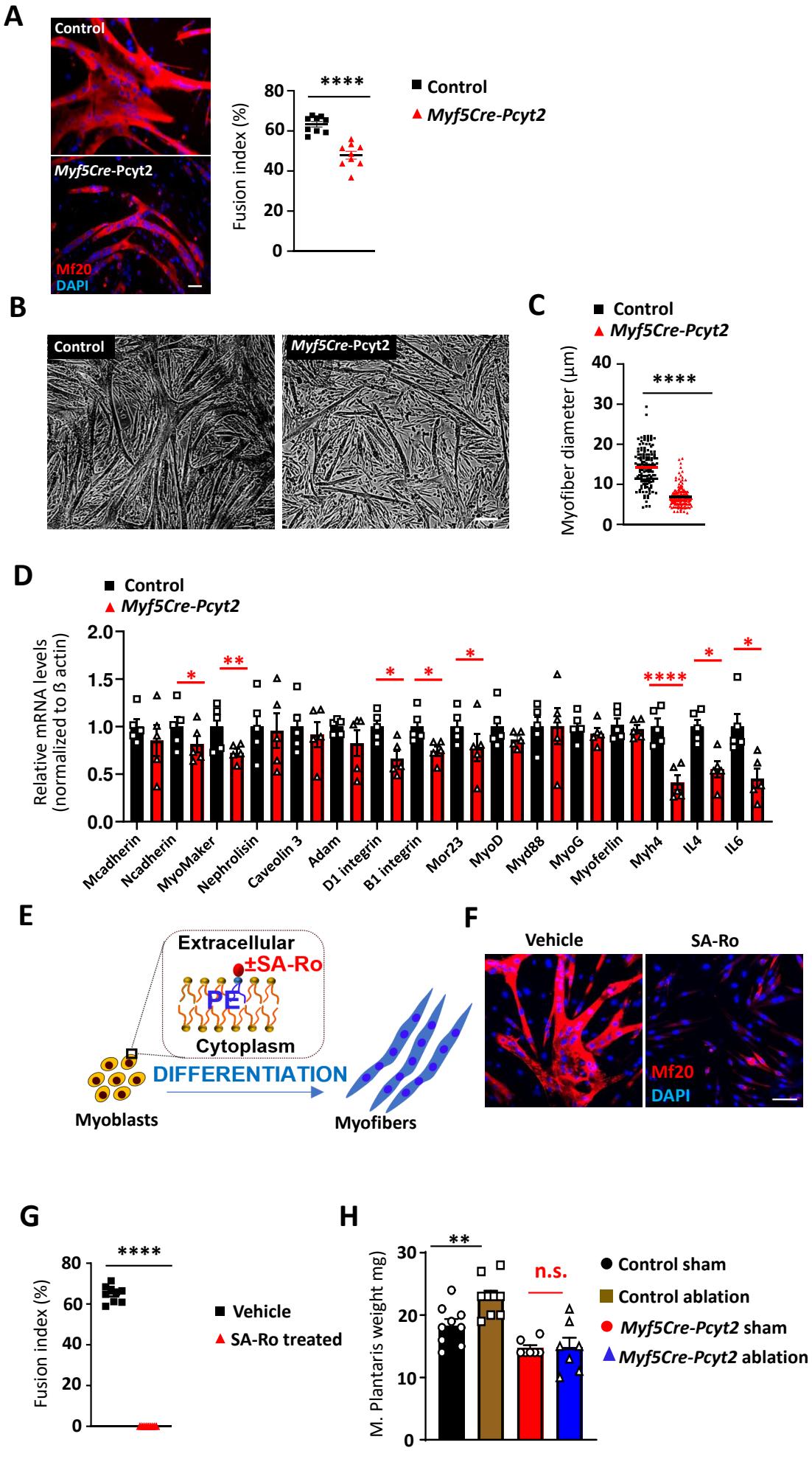
A
Control
Myf5Cre-Pcyt2
Mf20
DAPI
Fusion index (%)
****
Control
Myf5Cre-Pcyt2
B
Control
Myf5Cre-Pcyt2
C
Control
Myf5Cre-Pcyt2
Myofiber diameter (µm)
****
D
Control
Myf5Cre-Pcyt2
Relative mRNA levels (normalized to ß actin)
Mcadherin
Ncadherin
MyoMaker
Nephrolisin
Caveolin 3
Adam
D1 integrin
B1 integrin
Mor23
MyoD
Myd88
MyoG
Myoferlin
Myh4
IL4
IL6
E
Extracellular
±SA-Ro
PE
Cytoplasm
DIFFERENTIATION
Myoblasts
Myofibers
F
Vehicle
SA-Ro
Mf20
DAPI
G
Fusion index (%)
****
Vehicle
SA-Ro treated
H
M. Plantaris weight mg
**
n.s.
Control sham
Control ablation
Myf5Cre-Pcyt2 sham
Myf5Cre-Pcyt2 ablation

Figure 3

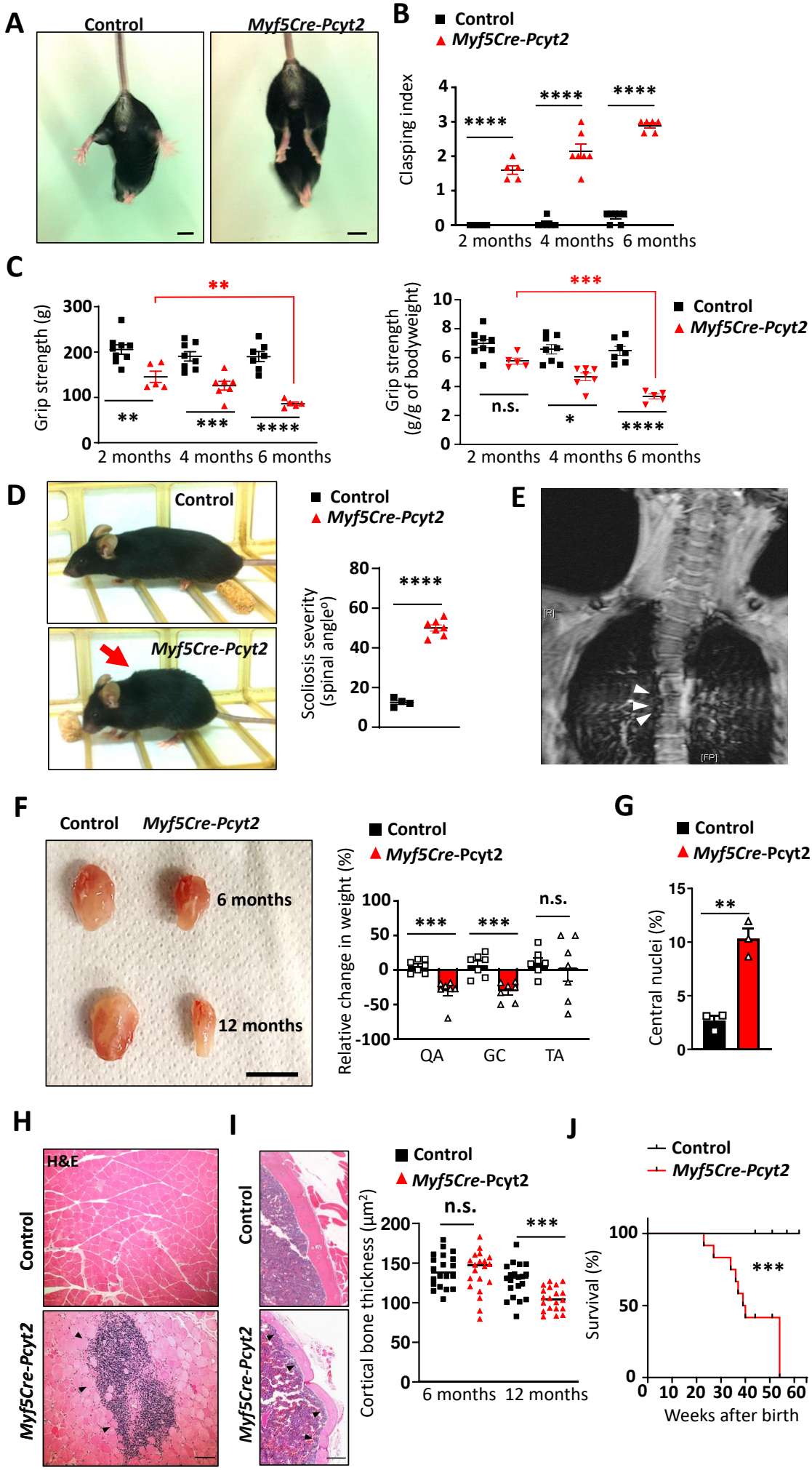
A
Control
Myf5Cre-Pcyt2
B
Control
Myf5Cre-Pcyt2
Clasping index
2 months 4 months 6 months
C
Grip strength (g)
Grip strength (g/g of bodyweight)
n.s.
D
Control
Myf5Cre-Pcyt2
Scoliosis severity (spinal angle°)
E
F
6 months
12 months
Relative change in weight (%)
QA GC TA
G
Central nuclei (%)
H
H&E
I
Cortical bone thickness (µm²)
J
Survival (%)
Weeks after birth

Figure 4

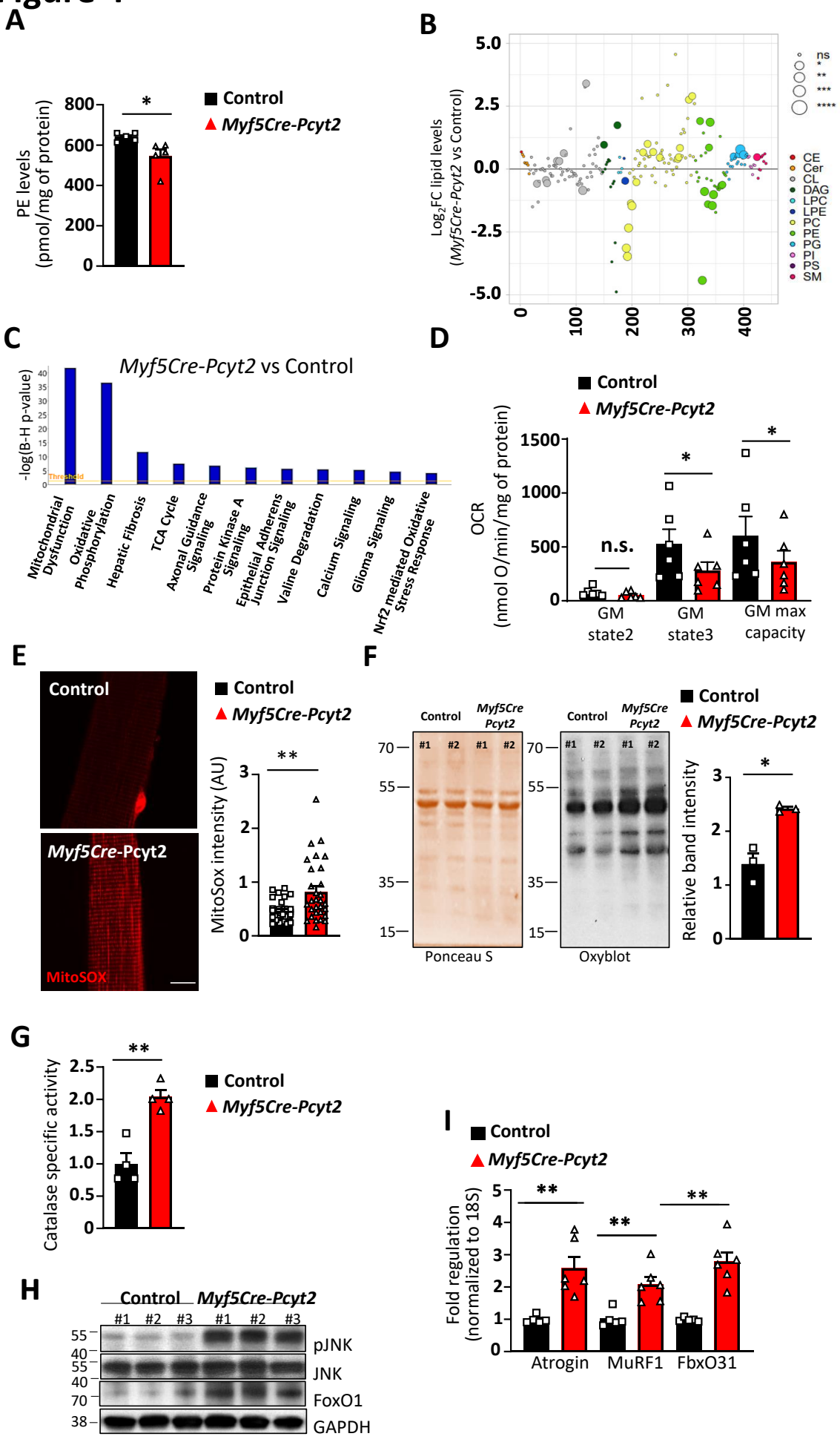
A
PE levels (pmol/mg of protein)
Control
Myf5Cre-Pcyt2
B
Log2FC lipid levels (Myf5Cre-Pcyt2 vs Control)
ns
CE
Cer
CL
DAG
LPC
LPE
PC
PE
PG
PI
PS
SM
C
Myf5Cre-Pcyt2 vs Control
-log(B-H p-value)
Mitochondrial Dysfunction
Oxidative Phosphorylation
Hepatic Fibrosis
TCA Cycle
Axonal Guidance Signaling
Protein Kinase A Signaling
Epithelial Adherens Junction Signaling
Valine Degradation
Calcium Signaling
Glioma Signaling
Nrf2 mediated Oxidative Stress Response
D
OCR (nmol O/min/mg of protein)
n.s.
GM state2
GM state3
GM max capacity
E
Control
Myf5Cre-Pcyt2
MitoSox intensity (AU)
MitoSOX
F
Ponceau S
Oxyblot
Relative band intensity
G
Catalase specific activity
H
pJNK
JNK
FoxO1
GAPDH
I
Fold regulation (normalized to 18S)
Atrogin
MuRF1
FbxO31

Figure 5

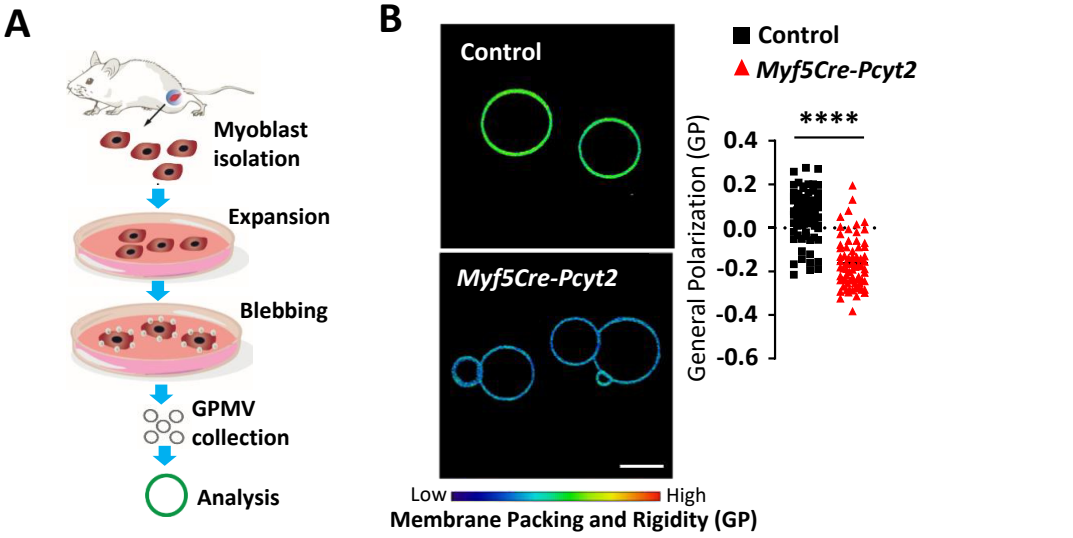
A
Myoblast isolation
Expansion
Blebbing
GPMV collection
Analysis
B
Control
Myf5Cre-Pcyt2
Control
Myf5Cre-Pcyt2
****
General Polarization (GP)
0.4
0.2
0.0
-0.2
-0.4
-0.6
Low
High
Membrane Packing and Rigidity (GP)

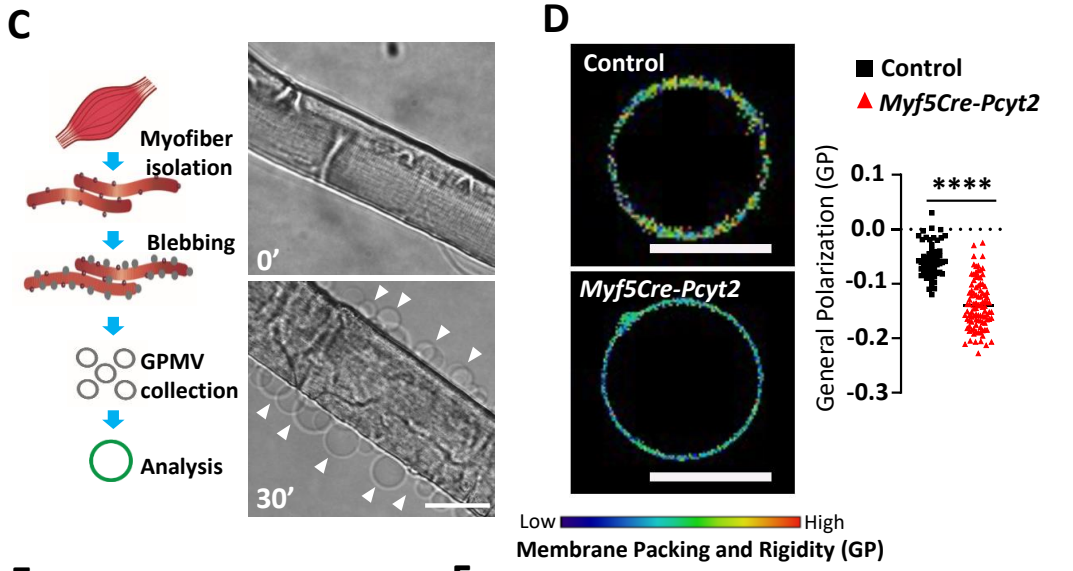
C
Myofiber isolation
Blebbing
GPMV collection
Analysis
0'
30'
D
Control
Myf5Cre-Pcyt2
Control
Myf5Cre-Pcyt2
****
General Polarization (GP)
0.1
0.0
-0.1
-0.2
-0.3
Low
High
Membrane Packing and Rigidity (GP)

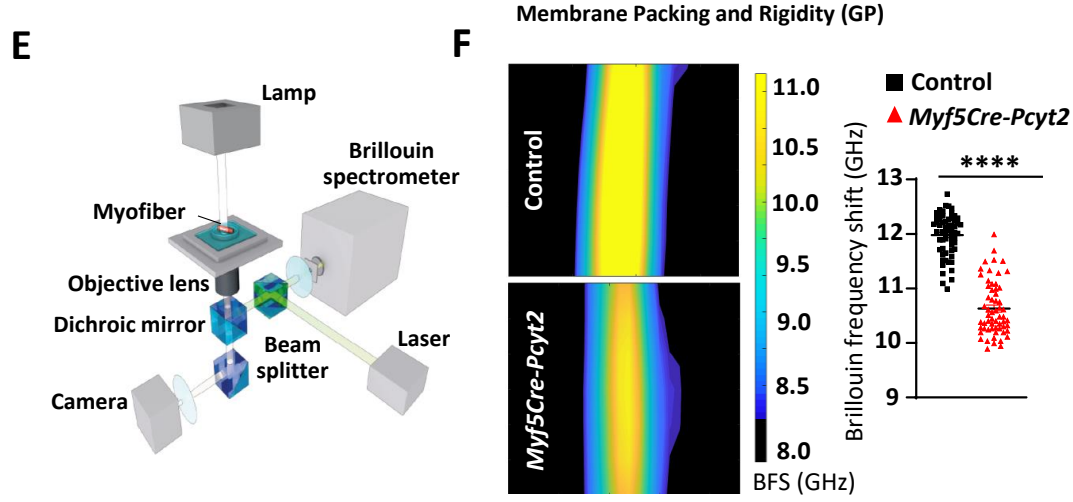
E
Lamp
Brillouin spectrometer
Myofiber
Objective lens
Dichroic mirror
Beam splitter
Laser
Camera
F
Control
Myf5Cre-Pcyt2
11.0
10.5
10.0
9.5
9.0
8.5
8.0
BFS (GHz)
Control
Myf5Cre-Pcyt2
****
Brillouin frequency shift (GHz)
13
12
11
10
9

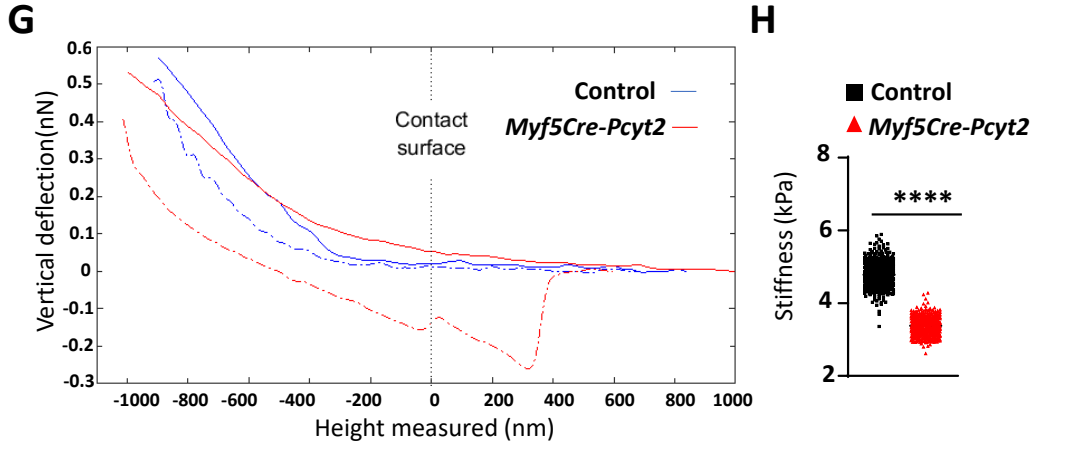
G
Vertical deflection(nN)
0.6
0.5
0.4
0.3
0.2
0.1
0
-0.1
-0.2
-0.3
Contact surface
Control
Myf5Cre-Pcyt2
-1000 -800 -600 -400 -200 0 200 400 600 800 1000
Height measured (nm)
H
Control
Myf5Cre-Pcyt2
****
Stiffness (kPa)
8
6
4
2

Figure 6

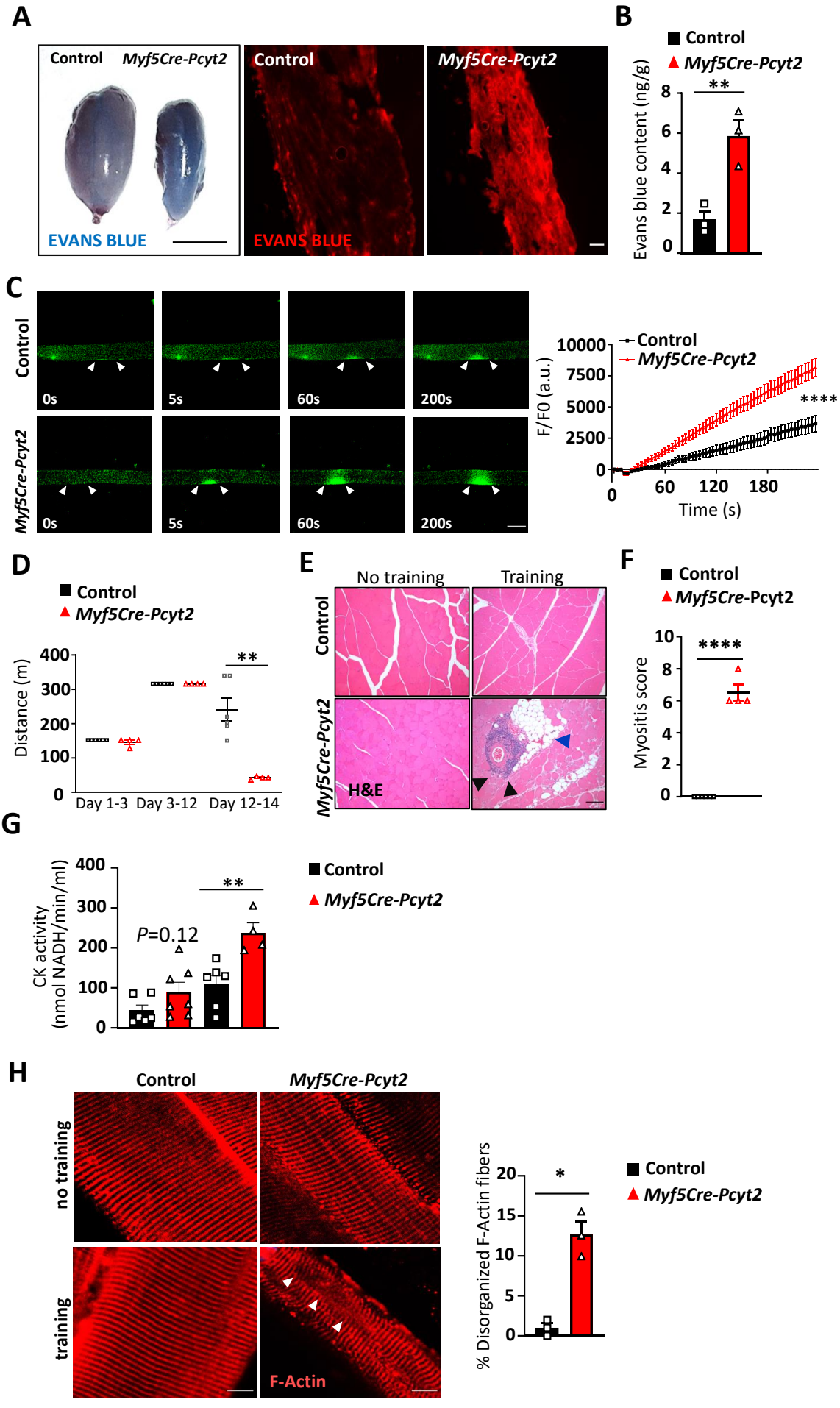
A
Control
Myf5Cre-Pcyt2
EVANS BLUE
Control
Myf5Cre-Pcyt2
EVANS BLUE
B
Control
Myf5Cre-Pcyt2
Evans blue content (ng/g)
**
C
Control
Myf5Cre-Pcyt2
0s
5s
60s
200s
F/FO (a.u.)
Time (s)
****
D
Control
Myf5Cre-Pcyt2
Distance (m)
**
Day 1-3
Day 3-12
Day 12-14
E
No training
Training
Control
Myf5Cre-Pcyt2
H&E
F
Control
Myf5Cre-Pcyt2
Myositis score
****
G
Control
Myf5Cre-Pcyt2
CK activity (nmol NADH/min/ml)
P=0.12
**
H
Control
Myf5Cre-Pcyt2
no training
training
F-Actin
% Disorganized F-Actin fibers
*
Control
Myf5Cre-Pcyt2

Figure 7

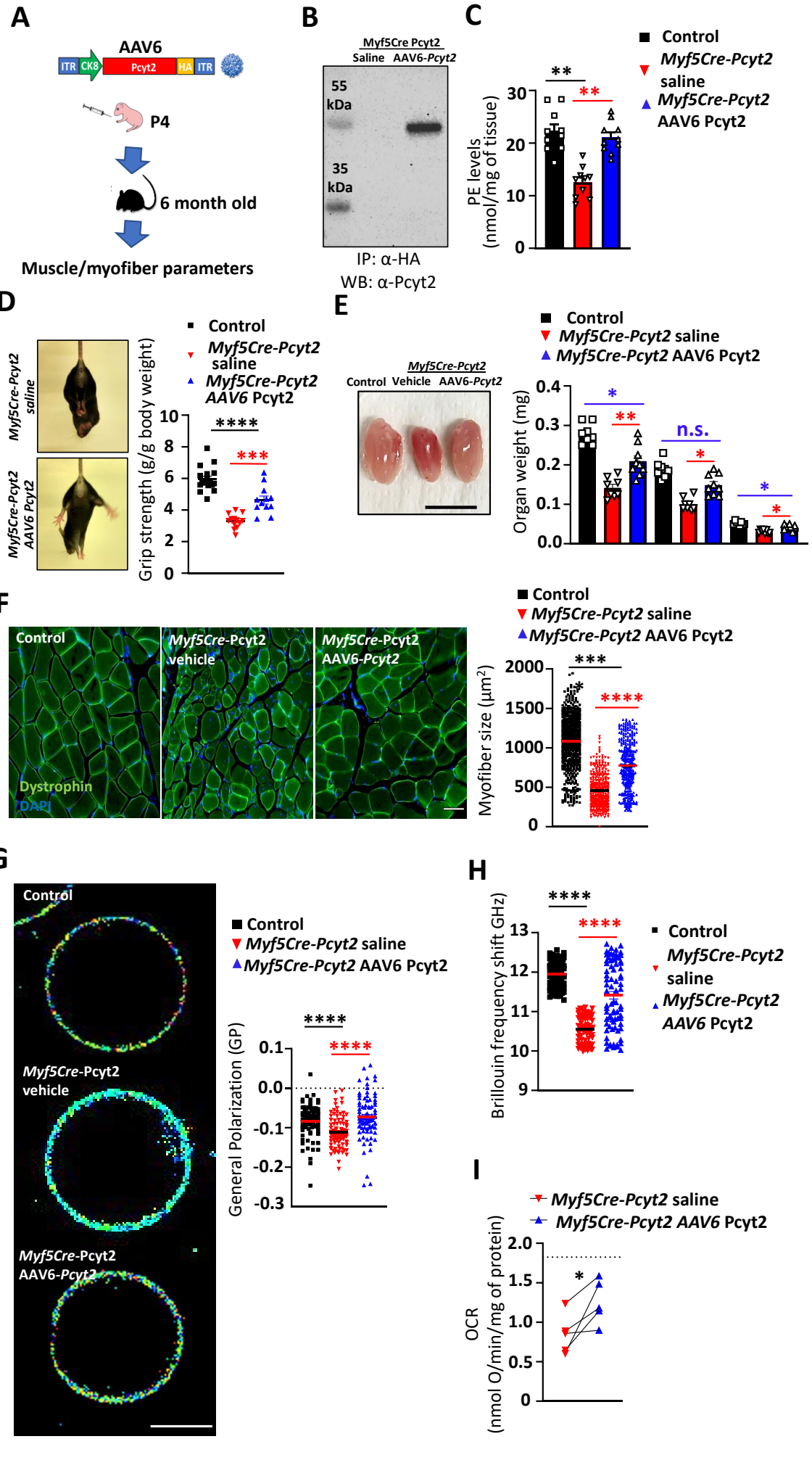
A
AAV6
ITR
CK8
Pcyt2
HA
ITR
P4
6 month old
Muscle/myofiber parameters
B
Myf5Cre Pcyt2
Saline
AAV6-Pcyt2
55 kDa
35 kDa
IP: α-HA
WB: α-Pcyt2
C
Control
Myf5Cre-Pcyt2 saline
Myf5Cre-Pcyt2 AAV6 Pcyt2
PE levels (nmol/mg of tissue)
D
Myf5Cre-Pcyt2 saline
Myf5Cre-Pcyt2 AAV6 Pcyt2
Grip strength (g/g body weight)
E
Myf5Cre-Pcyt2
Control
Vehicle
AAV6-Pcyt2
Organ weight (mg)
n.s.
F
Control
Myf5Cre-Pcyt2 vehicle
Myf5Cre-Pcyt2 AAV6-Pcyt2
Dystrophin
DAPI
Myofiber size (μm²)
G
Control
Myf5Cre-Pcyt2 vehicle
Myf5Cre-Pcyt2 AAV6-Pcyt2
General Polarization (GP)
H
Brillouin frequency shift GHz)
I
OCR (nmol O/min/mg of protein)

Figure 8

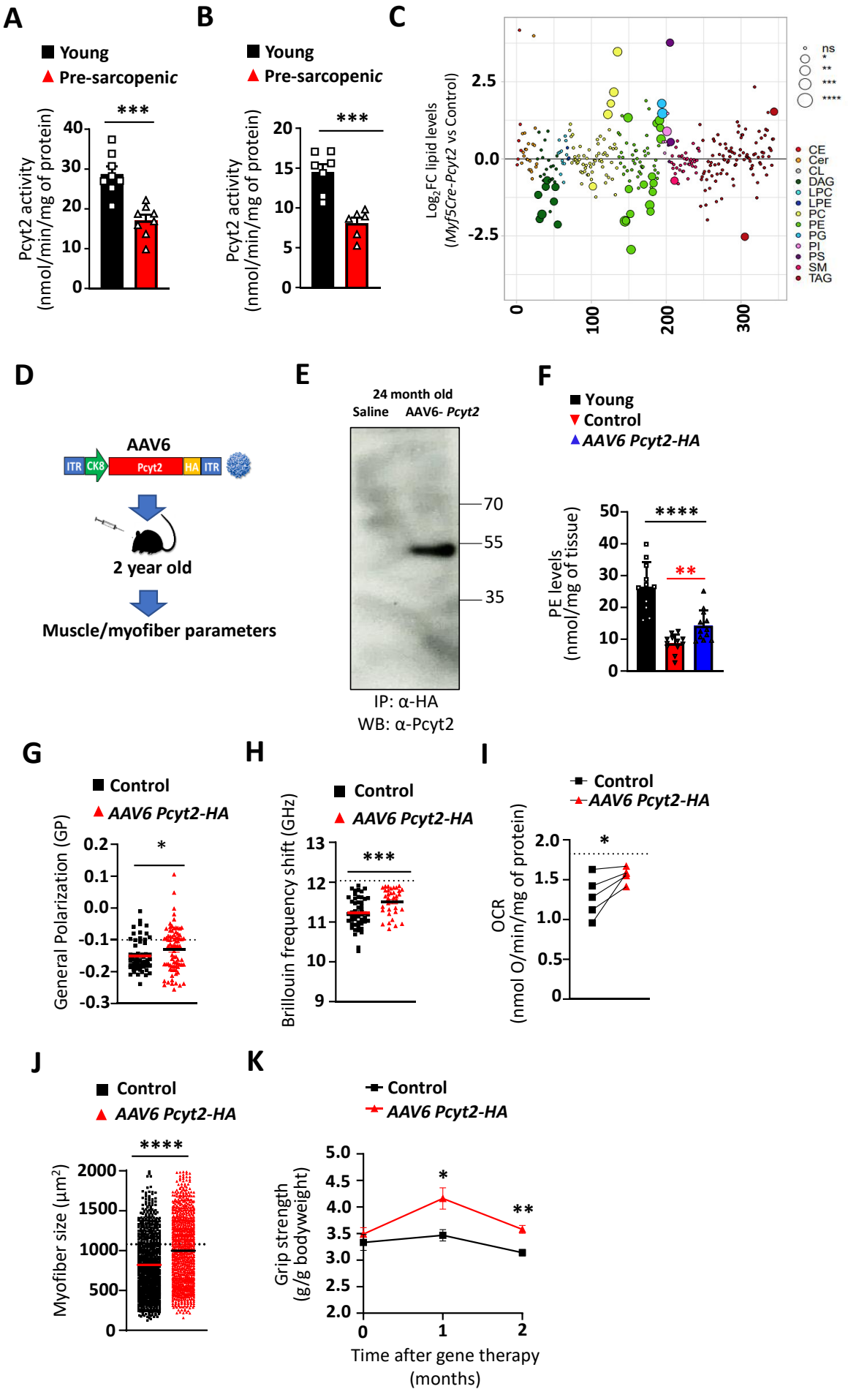
A
Young
Pre-sarcopenic
Pcyt2 activity (nmol/min/mg of protein)
***
B
Young
Pre-sarcopenic
Pcyt2 activity (nmol/min/mg of protein)
***
C
Log2FC lipid levels (Myf5Cre-Pcyt2 vs Control)
ns
*
**
***
****
CE
Cer
CL
DAG
LPC
LPE
PC
PE
PG
PI
PS
SM
TAG
D
AAV6
ITR
CK8
Pcyt2
HA
ITR
2 year old
Muscle/myofiber parameters
E
24 month old
Saline
AAV6- Pcyt2
70
55
35
IP: α-HA
WB: α-Pcyt2
F
Young
Control
AAV6 Pcyt2-HA
PE levels (nmol/mg of tissue)
****
**
G
Control
AAV6 Pcyt2-HA
General Polarization (GP)
*
H
Control
AAV6 Pcyt2-HA
Brillouin frequency shift (GHz)
***
I
Control
AAV6 Pcyt2-HA
OCR (nmol O/min/mg of protein)
*
J
Control
AAV6 Pcyt2-HA
Myofiber size (µm2)
****
K
Control
AAV6 Pcyt2-HA
Grip strength (g/g bodyweight)
*
**
Time after gene therapy (months)

Extended Data Figure 1

A

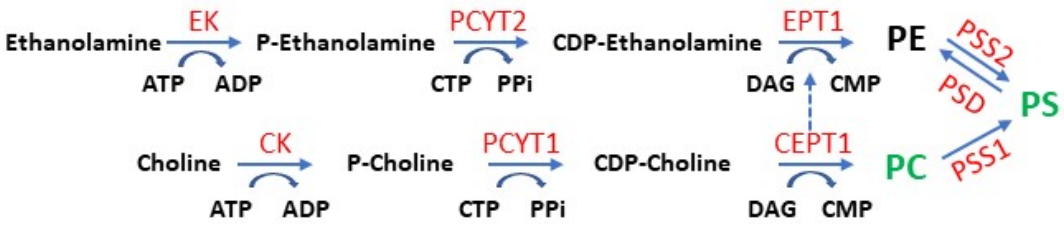

B

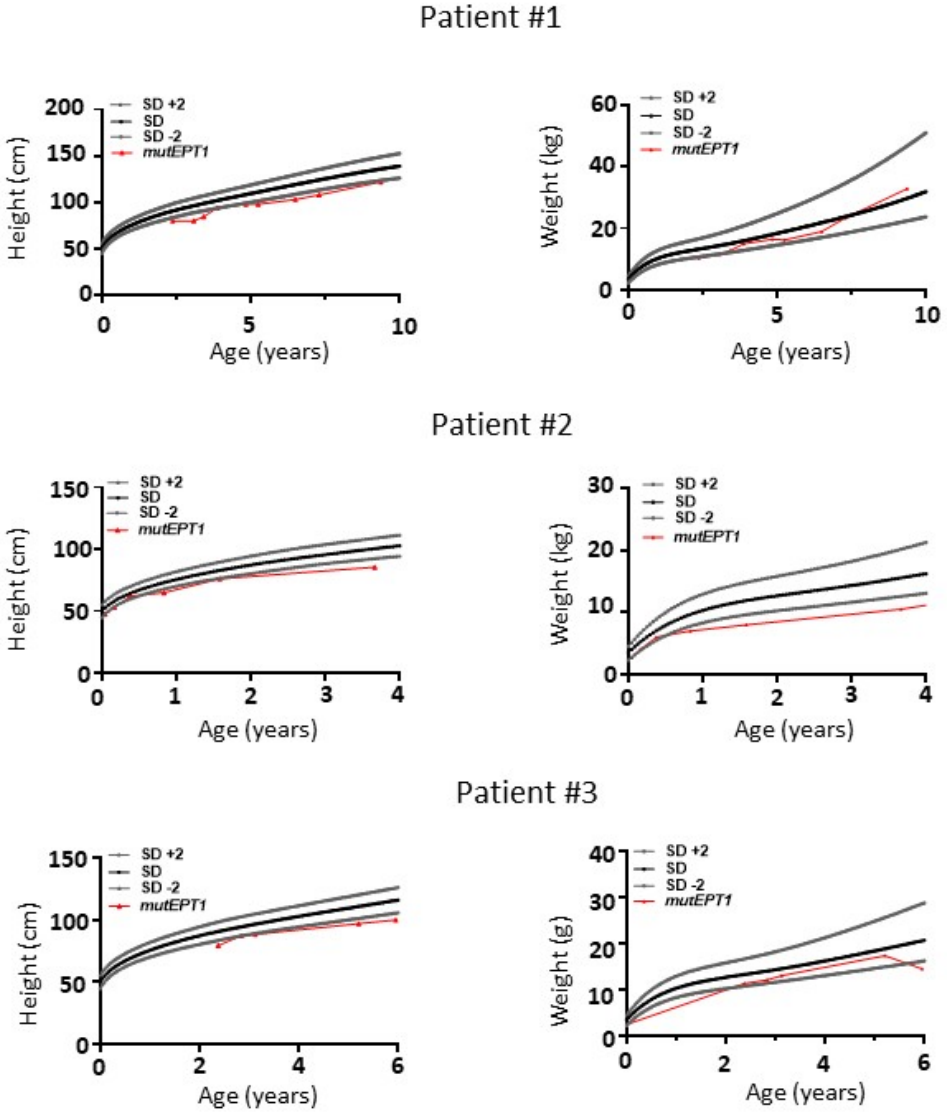

Extended Data Figure 2

A

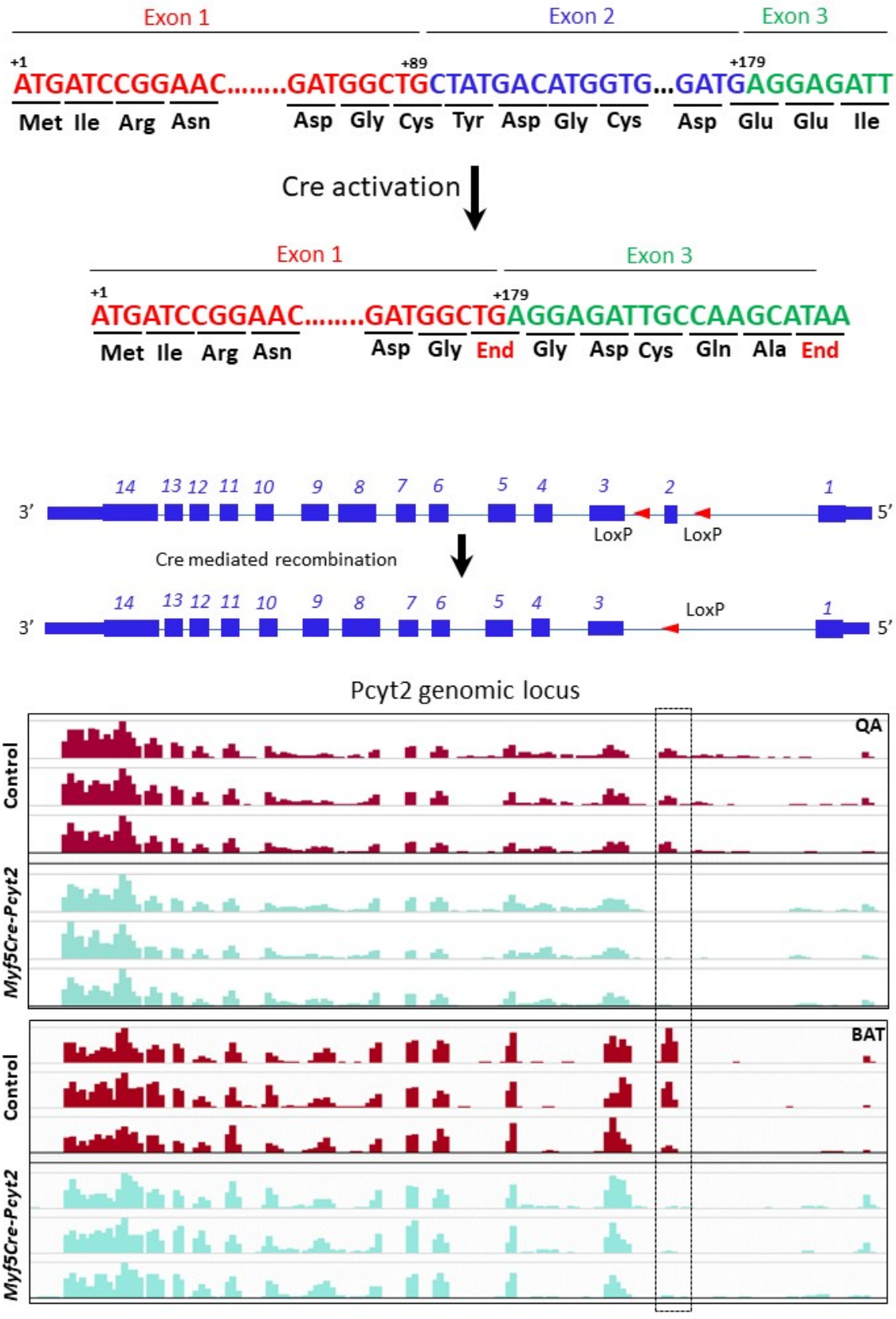

Extended Data Figure 3

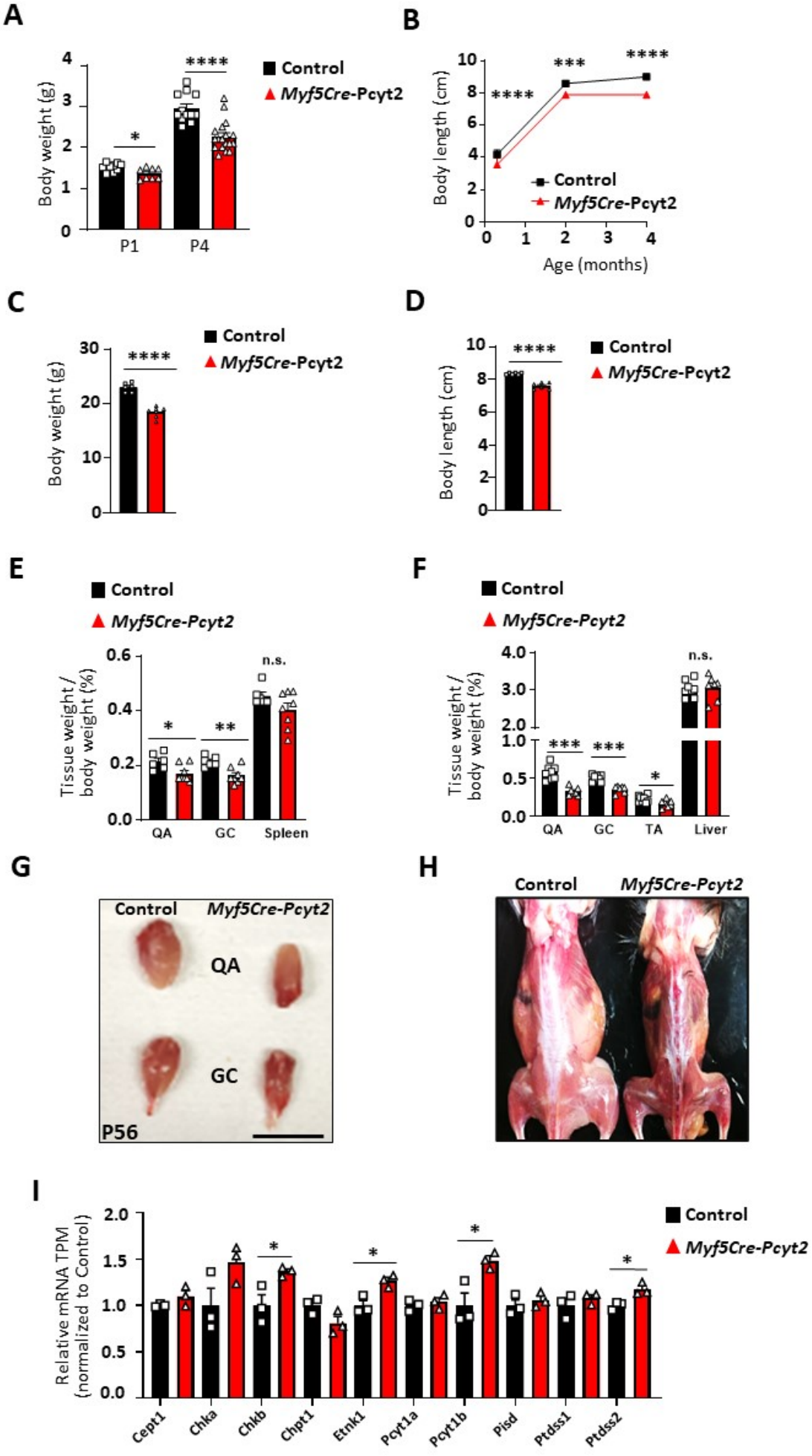

Extended Data Figure 4

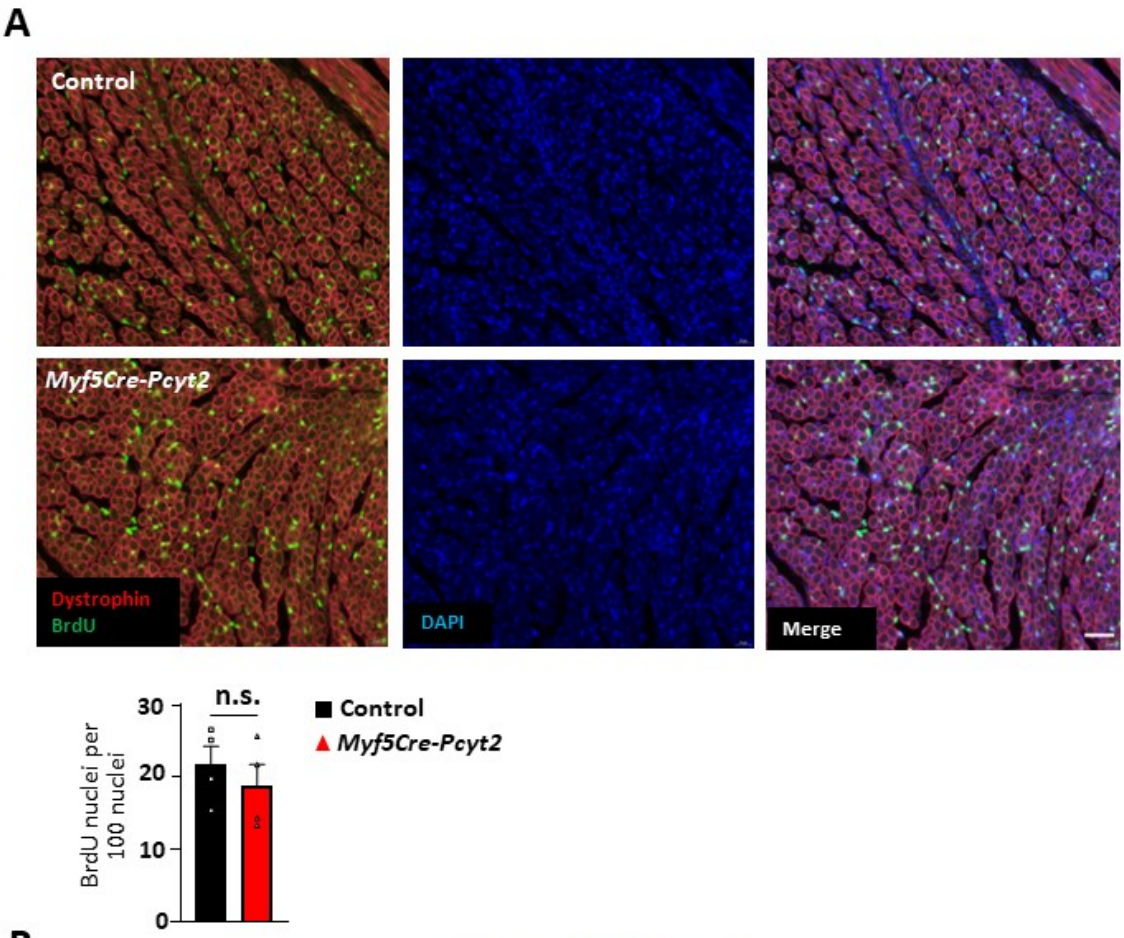

Extended Data Figure 5

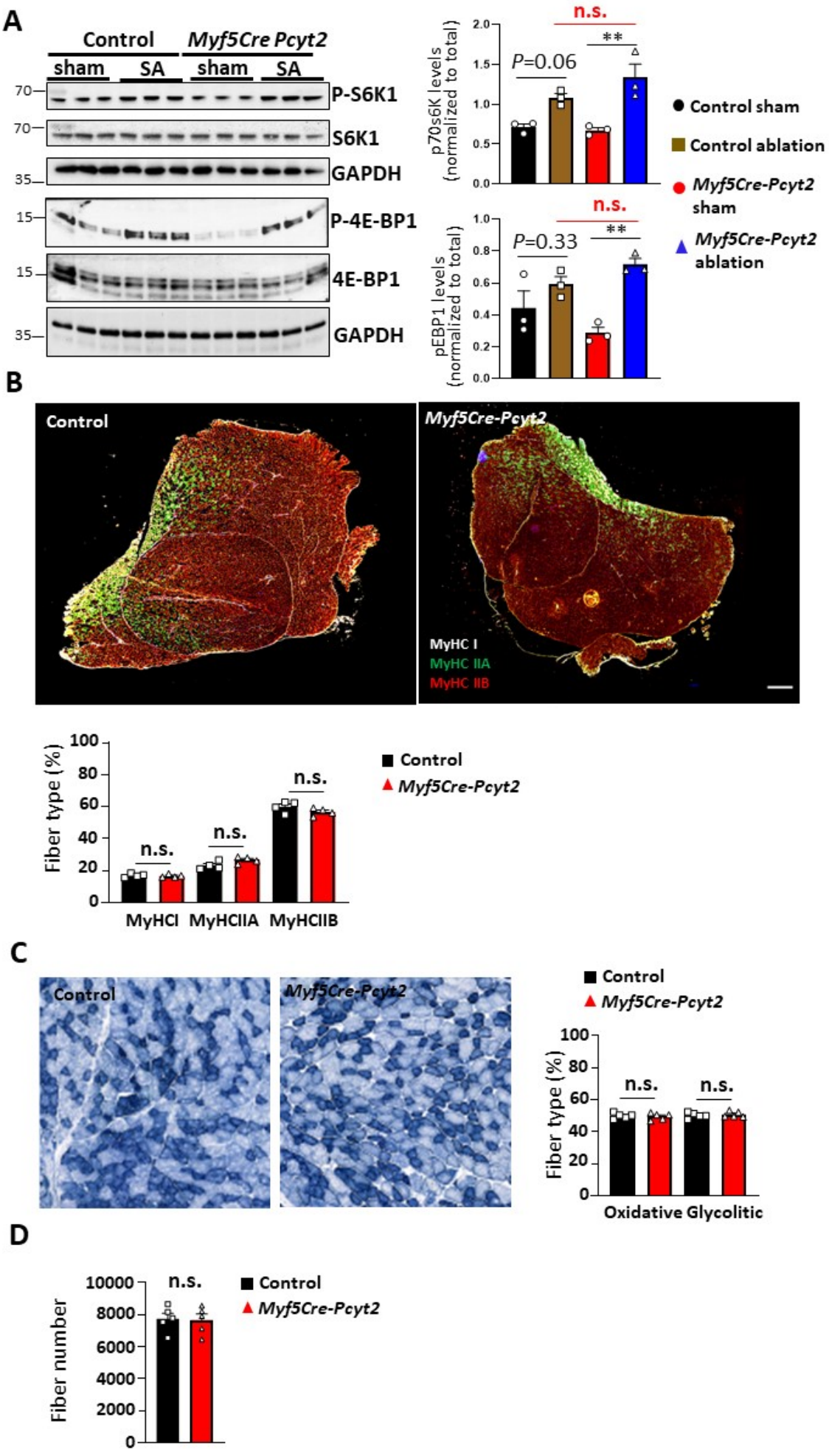

Extended Data Figure 6

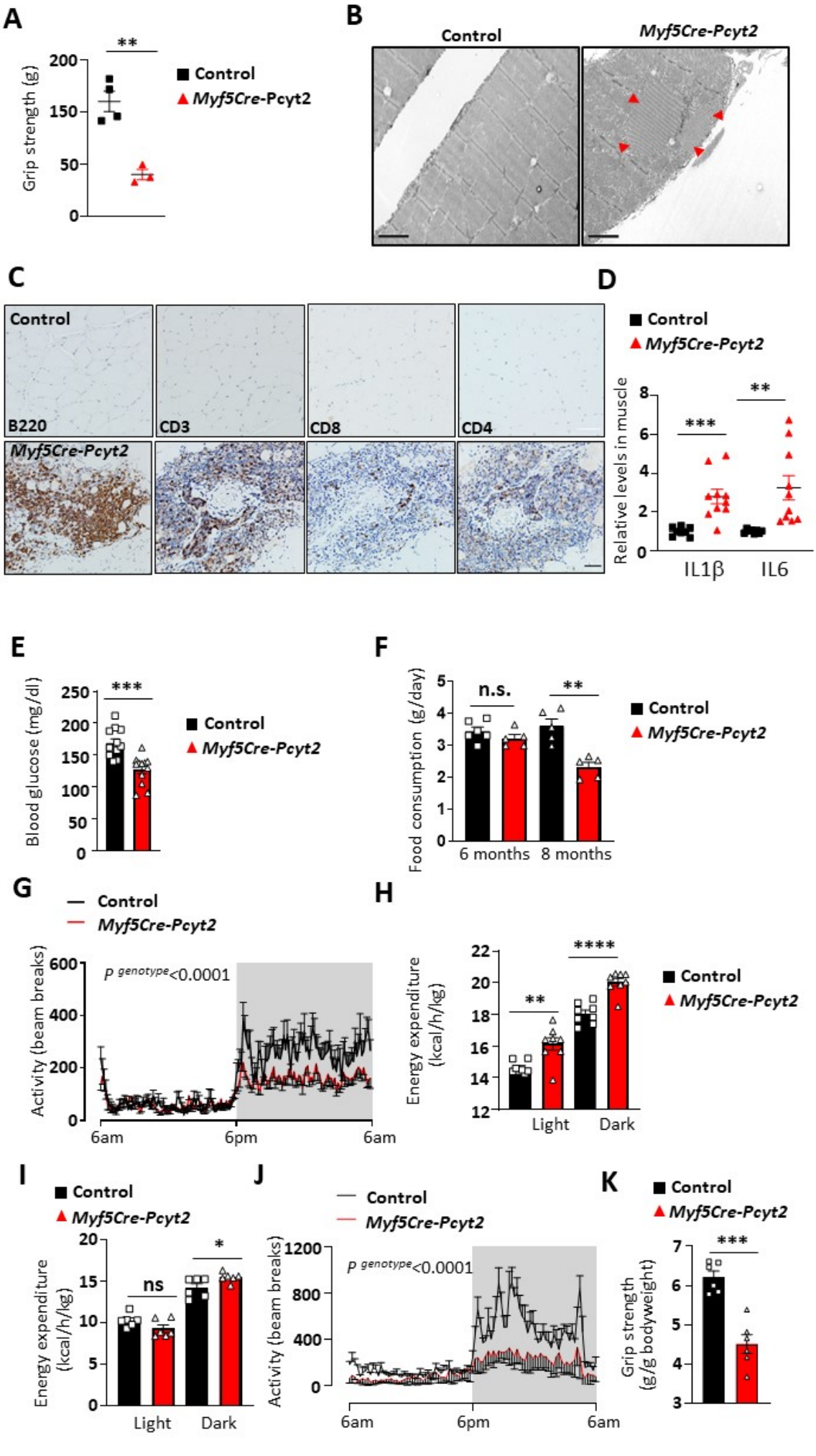

Extended Data Figure 7

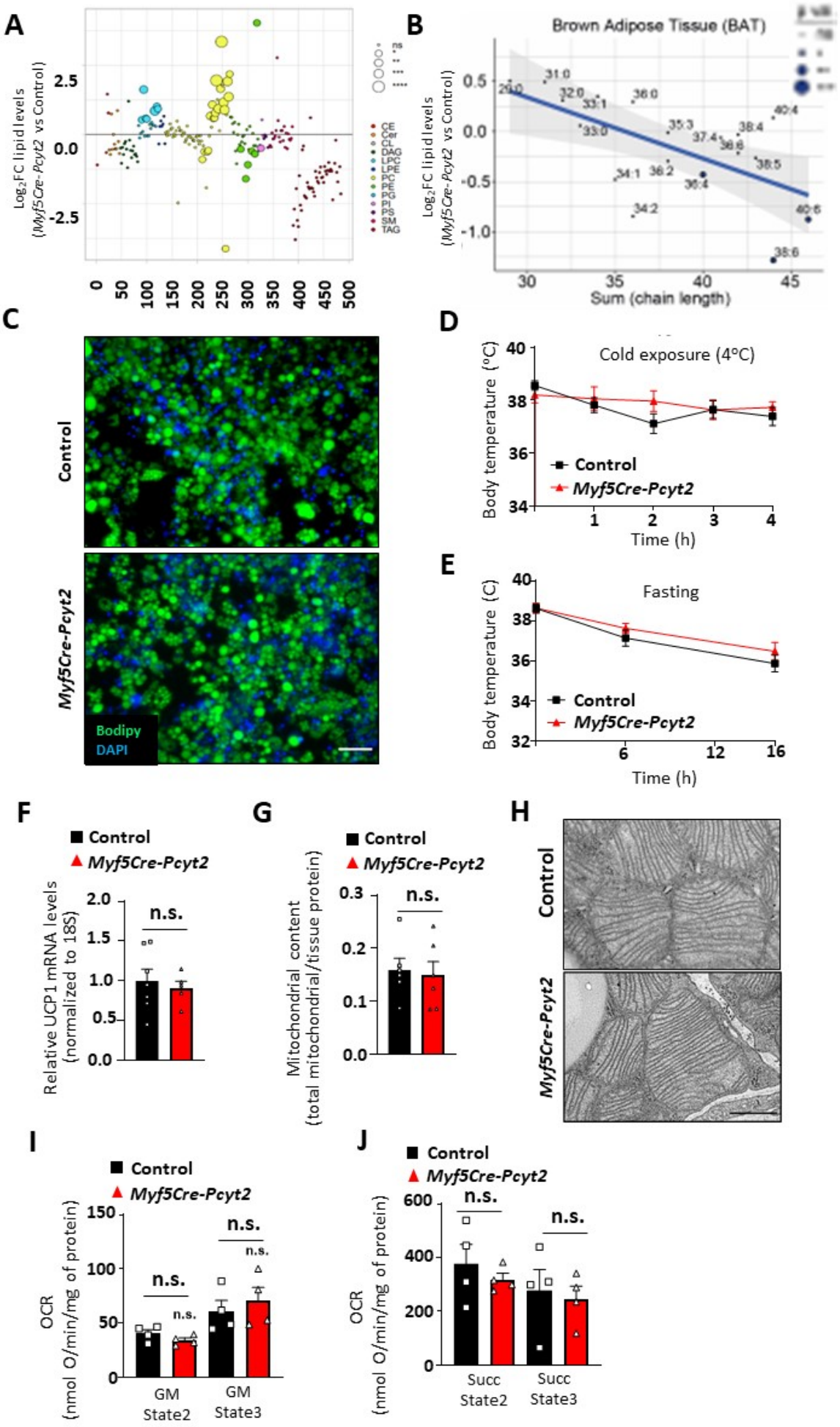

Extended Data Figure 8

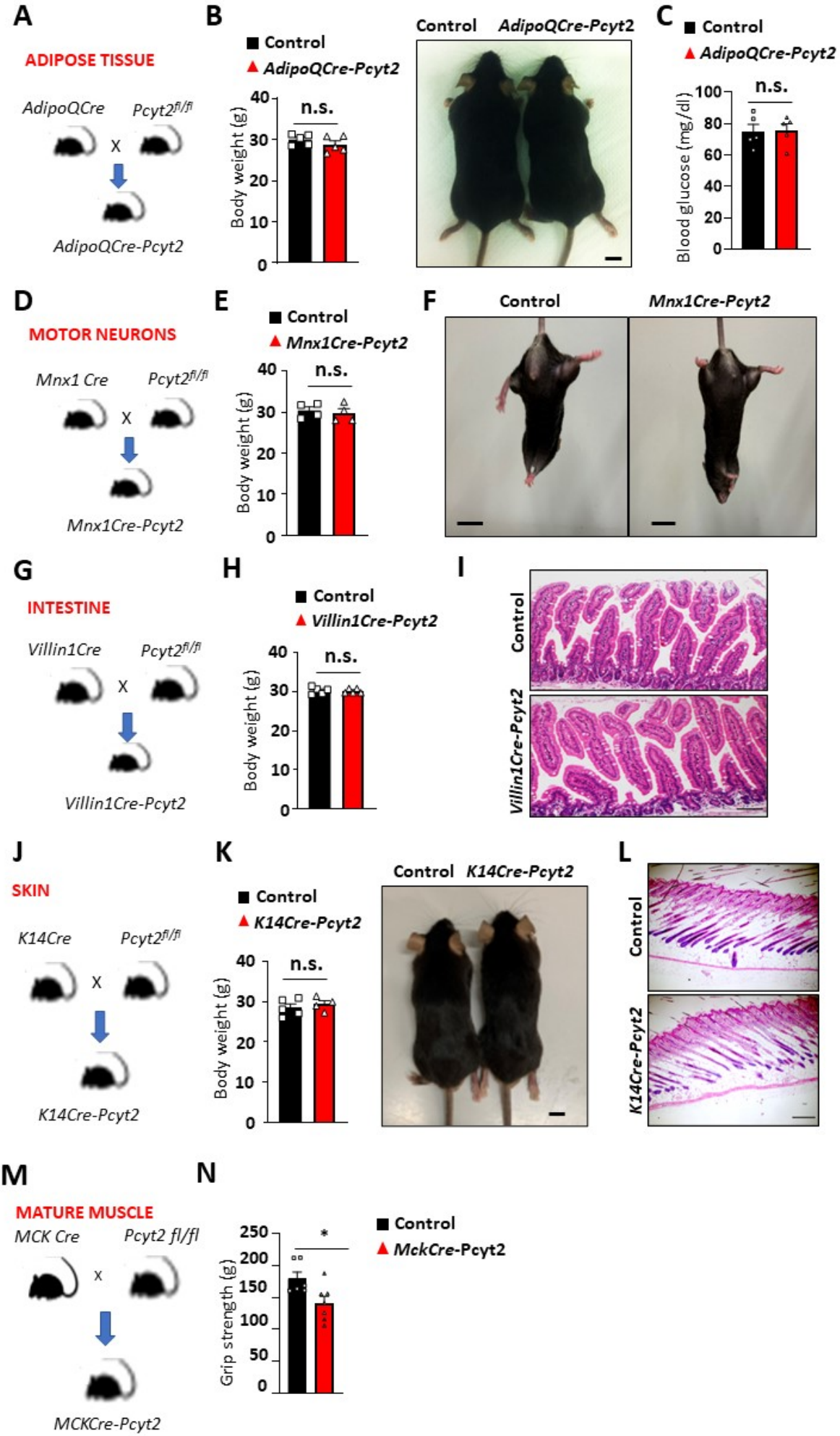

Extended Data Figure 9

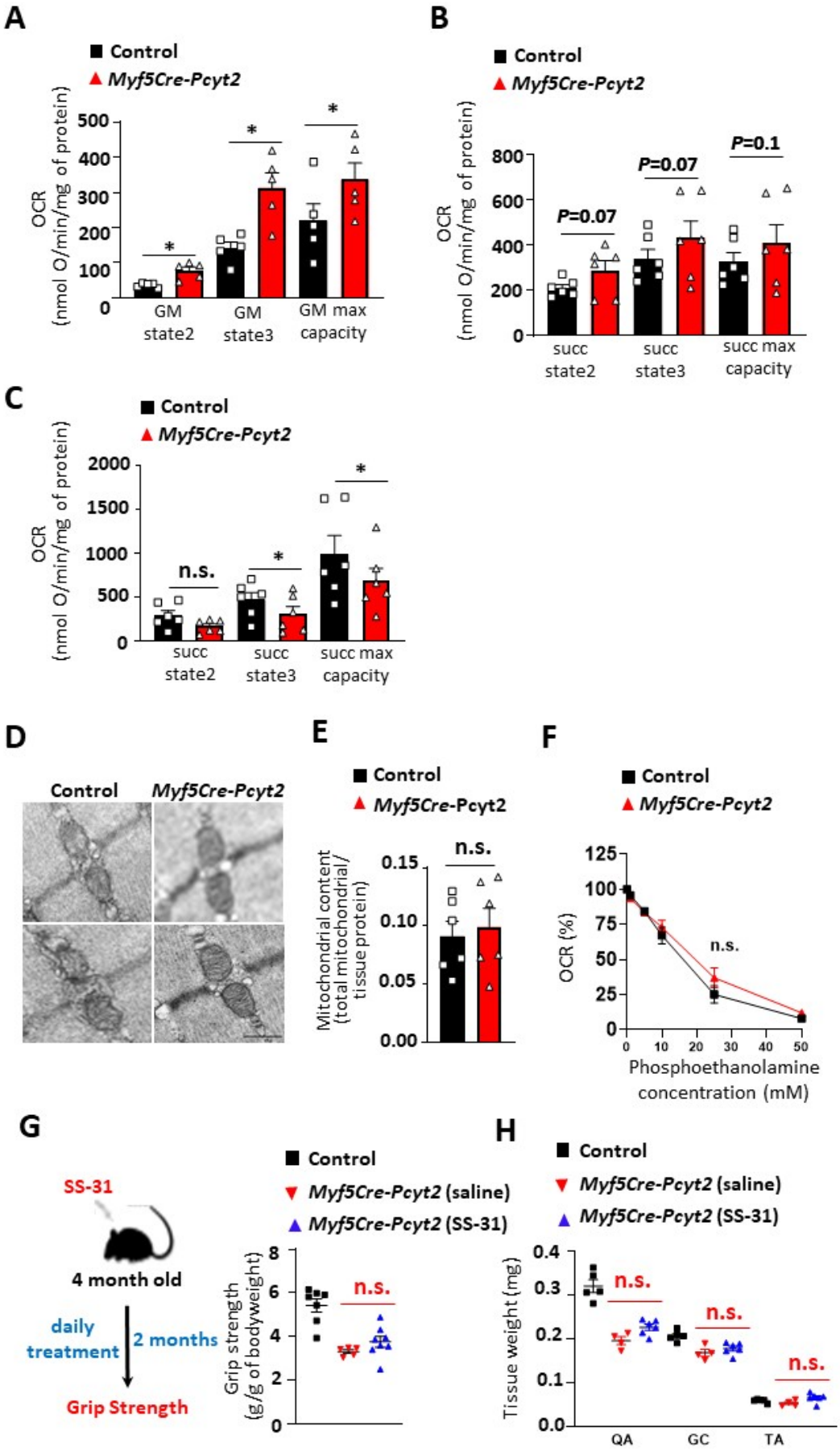

Extended Data Figure 10